Oxygen Sensing

International Edition: DOI: 10.1002/anie.201410646
German Edition: DOI: 10.1002/ange.201410646

Oxygen-Sensing Methods in Biomedicine from the Macroscale to the Microscale

*Emmanuel Roussakis, Zongxi Li, Alexander J. Nichols, and Conor L. Evans**

Keywords:
hypoxia · molecular imaging · oxygen sensing · phosphorescence quenching · tissue oxygenation

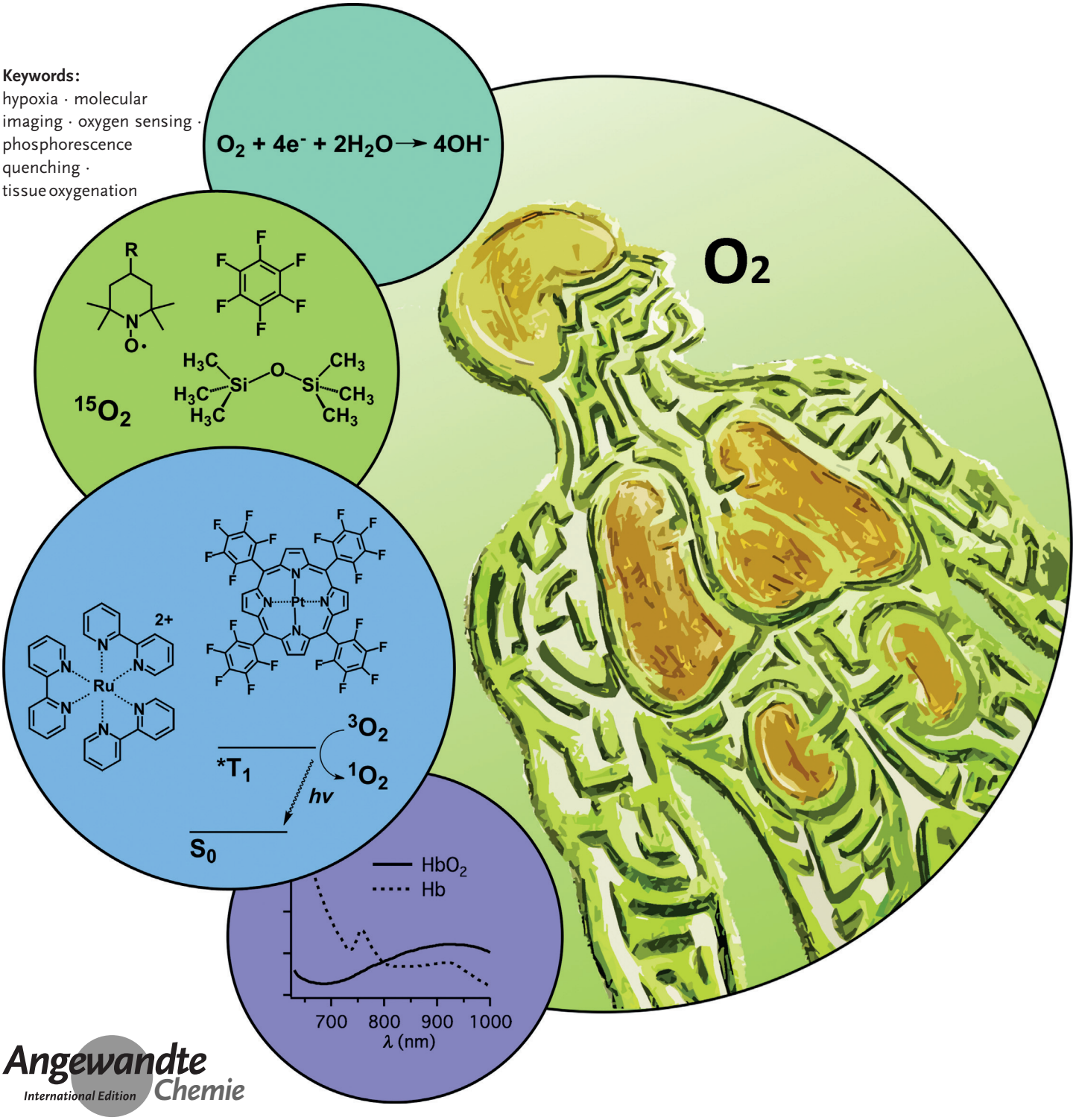

Oxygen monitoring has been a topic of exhaustive study given its central role in the biochemistry of life. The ability to quantify the physiological distribution and real-time dynamics of oxygen from subcellular to macroscopic levels is required to fully understand the mechanisms associated with both normal physiology and disease states. This Review will present the most significant recent advances in the development of oxygen-sensing materials and techniques, including polarographic, nuclear medicine, magnetic resonance, and optical approaches, that can be applied specifically for the real-time monitoring of oxygen dynamics in cellular and tissue environments. As some of the most exciting recent advances in synthetic methods and biomedical applications have been in the field of optical oxygen sensors, a major focus will be on the development of these toolkits.

From the Contents

1. Introduction	8341
2. Polarographic Electrodes	8343
3. Radioisotope Techniques	8344
4. Resonance Techniques	8345
5. Optical Methods for the Hemoglobin-Based Assessment of Oxygen Saturation	8348
6. Oxygen Sensing Based on Luminescence Quenching	8349
7. Conclusions and Outlook	8357

1. Introduction

1.1. The Importance of Oxygen

As one of the primary constituents of the Earth's atmosphere, molecular oxygen is ubiquitous in living systems and essential to the existence of all known higher organisms. Mammals have evolved complex and adaptive circulatory systems that deliver oxygen throughout the body, while simultaneously engaging biological fail-safe mechanisms to prevent its toxic derivatives from escaping and causing cellular damage. Impaired oxygen delivery to tissue regions is etiologically significant in a wide range of pathological conditions ranging from cancer therapeutic resistance to diabetic ulcers.

In spite of its profound biological and clinical importance, a limited number of effective methods exist for non-disruptively quantifying oxygen in its physiological milieu. The absorption and emission spectra of oxygen are poorly specific and difficult to assess in a biological context, and its most abundant isotopic form is not active for nuclear magnetic resonance studies. Even the "gold standard" of oxygen sensing, namely electrochemical measurements with needle-based probes, suffers from severe drawbacks, including the difficulty of probing large surface areas and the inherently disruptive nature of the instrument and the measurement process. Furthermore, large oxygen concentration gradients are believed to exist within even a single organ or granular structure, necessitating the ability to quantify molecular oxygen at the tissue, cellular, and subcellular level to study the profound impact of this simple molecule on physiology and disease.

To contextualize the importance of oxygen measurements in both normal physiology as well as pathological states, we begin with a brief review of physiological oxygen tensions throughout the body and a discussion of the involvement of oxygen in disease states such as cancer. Afterwards, we will provide a review on polarographic, nuclear medicine, resonance, and optical methods that are under active research for sensing oxygen on the cellular and tissue levels.

1.2. Overview: Mechanisms of Oxygen Consumption, Utilization, and Metabolic Regulation

To understand the effects of reduced or impaired oxygen delivery in cells and tissues, it is first necessary to define basal levels of oxygenation while appreciating the heterogeneity that exists throughout healthy human organs. Under normal atmospheric conditions (i.e., room air), oxygen constitutes roughly 21% of air by volume, corresponding to a partial pressure of 158 mmHg. Under standard cell culture conditions, this number is often reduced to 150 mmHg owing to the addition of 5% CO_2 for pH control. During inspiration in a healthy individual, the oxygen partial pressure (pO_2) drops to approximately 100–110 mmHg in the alveoli, the functional units of air exchange within the lung.[1] After diffusing across the lung epithelium, oxygen encounters deoxygenated venous blood, which then becomes oxygenated and enters arterial circulation. In a healthy adult, the pO_2 values of arterial and venous blood (ca. 90 and 40 mmHg, respectively) are generally considered proxies for the pO_2 of blood on either side of the pulmonary vasculature and are thus important clinical parameters.[1]

Downstream of arterial circulation, there exists substantial variability in physiological oxygen tensions in solid organs. For example, the brain's dense neuronal parenchyma

[*] Dr. E. Roussakis, Dr. Z. Li, Dr. A. J. Nichols, Prof. Dr. C. L. Evans
Wellman Center for Photomedicine
Massachusetts General Hospital CNY 149-3210
13th Street, Charlestown, MA 02129 (USA)
E-mail: evans.conor@mgh.harvard.edu
Dr. A. J. Nichols, Prof. Dr. C. L. Evans
Harvard University Program in Biophysics
Building C2 Room 112
240 Longwood Avenue, Boston, MA 02115 (USA)
Dr. A. J. Nichols
Harvard-MIT Division of Health Sciences and Technology
77 Massachusetts Avenue E25-519
Cambridge, MA 02139 (USA)

is extraordinarily metabolically active, such that its oxygen consumption rates are high; oxygen tensions in the frontal white matter typically average 40 mmHg, but values ranging from 33 to 48 mmHg and beyond have been reported.[2,3] Likewise, muscle tissues exhibit pO_2 values of 25–32 mmHg, depending on the depth, muscle type, and muscle location.[2] Reported pO_2 values of the liver also exhibit a wide range and dependence on the physiological state. Whereas transplant recipients exhibit elevated liver pO_2 values of 60 mmHg 48 hours after the transplant, intraoperative pO_2 values recorded using a different method showed a median pO_2 value of 31 mmHg.[2,4] Therefore, physiological oxygen tensions can be highly heterogeneous and dependent on tissue function.

When considering these data, it is important to note that such large variances in the reported values are in part due to a lack of a commonly accepted, reliable approach for measuring the tissue oxygenation. Many of these were developed using point-based electrochemical methods, which are inherently limiting and of debatable utility in the solid organ environment. It is also important to note that these values reflect solid-tissue pO_2 values, as opposed to arterial pO_2 values measured in the organ-associated vasculature.

1.3. Tissue Hypoxia

In general, hypoxia in the biological sense is defined as a physiological state wherein the equilibrium pO_2 value within a tissue or cell is insufficient to meet the oxygen demands of that tissue. Interestingly, recent results suggest that there are important exceptions to this rule, where hypoxia may not always represent a pathological state. Bone marrow, for example, has been measured to be in the hypoxic regime (<20 mmHg), and some believe this low pO_2 value to be essential for normal hematopoiesis.[5–7] To appreciate the need for tissue-based oxygen sensors and the sensing range over which they must operate, it is thus essential to both define hypoxia quantitatively and physiologically as well as to understand how and when insufficient amounts of oxygen can be damaging to tissues. Oxygen homeostasis in a given tissue is fundamentally a function of two parameters: oxygen supply and demand. In the heart, for example, the myocardial oxygen demand is determined through a number of factors, including the heart rate and the contractility of each heart beat.[8,9] When one or more regulatory elements in this system become compromised (for example, by reduced coronary blood flow secondary to atherosclerosis and vessel stenosis), the heart exhibits changes on both the cellular and organ level. Although the pO_2 level at which this process occurs remains unclear, in part owing to the lack of reliable measurement techniques, studies suggest that the ischemic

Emmanuel Roussakis received his Ph.D. in Synthetic Organic Chemistry from the University of Crete (Greece) under the supervision of Dr. Haralambos Katerinopoulos in 2006. In 2008 he joined the group of Dr. Sergei Vinogradov at the Department of Biochemistry and Biophysics at the University of Pennsylvania's Perelman School of Medicine, where he worked on developing porphyrin-based oxygen probes with applications in the in vivo two-photon imaging of intravascular oxygen partial pressures. He currently works under Dr. Conor L. Evans at the Wellman Center of Photomedicine, developing brightly emissive oxygen-sensing probes that can be integrated into optical imaging methodologies for visualizing hypoxia in multicellular tumor models.

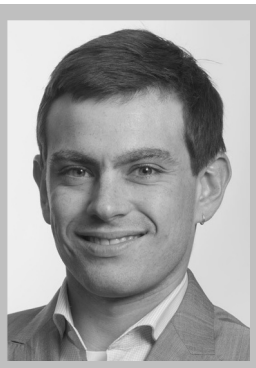

Alexander J. Nichols worked as a nanoparticle chemist at QDVIsion, Inc., and graduated from Oberlin College in 2008 in Biochemistry. He completed his Ph.D. in Biophysics in the Dr. Conor L. Evans group where he was enrolled in the Harvard/MIT Division of Health Sciences and Technology and worked in the Wellman Center for Photomedicine at Massachusetts General Hospital. He currently works as a biotechnology entrepreneur at Flagship Ventures in Cambridge, Massachusetts, where he works to translate breakthrough technologies into therapies for patients.

Zongxi Li received her Bachelor's Degree in Chemistry from Peking University, China in 2007 and her Ph.D. in Chemistry from the University of California, Los Angeles with Dr. Jeffrey I. Zink. Her doctoral research focused on the development of functional nanomaterials as advanced drug-delivery systems. In 2012, she joined the group of Dr. Conor L. Evans at the Wellman Center for Photomedicine at Massachusetts General Hospital. Her current research focuses on the development of biocompatible sensors and imaging systems for monitoring oxygen and other physiological parameters in humans.

Conor L. Evans received his degrees from Brown University (Bachelor of Science in Physical Chemistry) and Harvard University (Ph.D. in Chemistry with Dr. X. Sunney Xie). He carried out postdoctoral training with Tayyaba Hasan and Johannes de Boer (both at Massachusetts General Hospital) in the application of advanced microscopy to cancer research. He now serves as an Assistant Professor at the Wellman Center for Photomedicine of Harvard Medical School at the Massachusetts General Hospital. His research is focused on the development and clinical translation of optical microscopy and spectroscopy tools, with a specific interest in the synthesis of bright oxygen sensors that can be translated for clinical use.

threshold may be near 22 mmHg, with myocardial oxygen tensions falling to 6 mmHg or lower during severe hypoxic/ischemic episodes.[10–12]

1.4. Hypoxia and Cancer

Aside from its role in diseases of ischemic etiology, hypoxia is known to occur in tumors and is an important clinical factor in cancer-treatment planning and efficacy. As demonstrated in Figure 1, primary solid tumors become

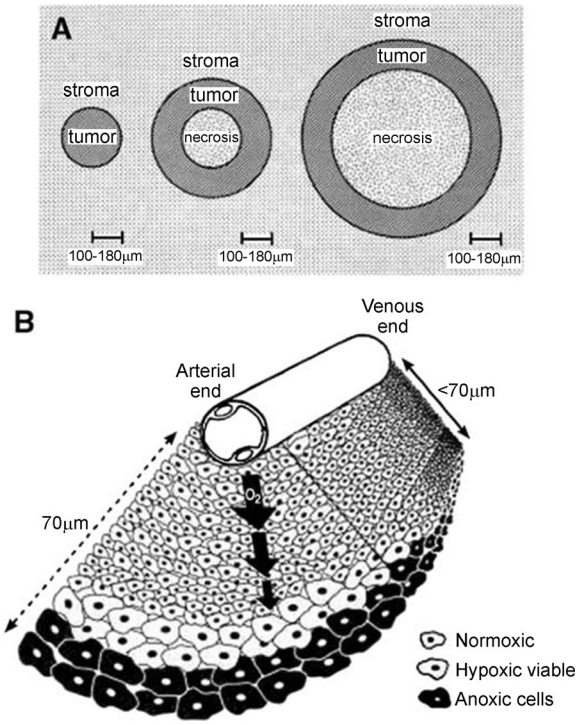

Figure 1. As tumors grow, they become starved of oxygen. A) During the growth of cancerous tissue, the demand for oxygen can outweigh the supply, leading to the formation of necrotic regions. B) Mismatches between the supply and demand of oxygen lead to the creation of hypoxic and anoxic regions surrounding the blood vessels. Reproduced with permission from Ref. [24].

hypoxic as they grow beyond the diffusion distance of oxygen from nearby vasculature (up to 200 μm).[13] The presence of hypoxia contributes to hypoxia-induced factor 1 (HIF-1) signaling leading to the transcription of genes, including the vascular endothelial growth factor (VEGF), which in turn stimulates the growth of new blood vessels in the vicinity of the tumor. The tumor-associated neovasculature is morphologically chaotic and leaky and often fails to deliver oxygen uniformly throughout the entirety of the tumor, thereby contributing to the formation of heterogeneous regions of hypoxia.[14–17] Once present, hypoxic conditions exert a plethora of tumor-promoting effects, including the suppression of apoptosis, an elevation of genomic instability secondary to hypoxia-induced reactive oxygen species (ROS) generation, enhanced invasiveness, the alteration of lipid metabolism, and the selection of somatic mutations favorable to survival in the hypoxic environment.[13,18] Clinically, hypoxia contributes to cancer resistance to numerous therapies, including the chemotherapeutics etoposide, 5-fluorouracil, paclitaxel, and doxorubicin, as well as to radiation therapy.[13,19–22] In some cases, the therapeutic resistance can be dramatic; for example, up to 100-fold decreases in paclitaxel cytotoxicity have been reported under hypoxic conditions.[23]

It is important to emphasize that heterogeneities in tumor oxygenation occur on the microenvironmental level, and can vary across clusters of cells or even across individual cells. This highlights the importance of understanding tumor oxygenation at all scales, from whole organs to tissues to individual cells.[19,25–27] This Review presents tissue oxygen sensing techniques across the macro- and microscales, including techniques based on polarographic electrodes, radioisotope labeling, nuclear and electronic resonance, optical measurements of O_2 saturation, and luminescence quenching. Table 1 provides an overview of these different types of techniques, summarizing the merits and limitations of each technique.

2. Polarographic Electrodes

Polarographic electrodes, which were introduced in the 1950s, were the first technology to allow for the accurate measurement of tissue oxygen levels. Polarographic oxygen electrodes (also known as Clark electrodes) measure the electric current formed at a cathode upon reduction of oxygen, with the generated current being directly proportional to pO_2.[28] The design generally includes a platinum electrode surrounded by a needle sheath made of glass or stainless steel, the tip of which is isolated from the environment by a gas-permeable membrane. The pO_2 measurements made by polarographic electrodes can be highly accurate, and the method is considered the gold standard for measuring tissue oxygenation.[51] However, their usage in humans is limited by their invasiveness, as the insertion of needle-based probes is less than tolerable in most clinical situations. Importantly, they must be properly calibrated for each environment, as environmental factors, such as temperature and ionic strength, affect the performance. Moreover, oxygen readings in tissues are highly location-dependent, with needle-induced damage to capillaries and small blood vessels further complicating the matter.[30] Furthermore, as the probe itself consumes oxygen during point measurements, taking repeated readings at a single tissue location can pose a challenge.

Optimizations to the conventional polarographic electrodes have been aimed at making them more suitable for tissue oxygen sensing. The Eppendorf electrode system, for example, has a computerized driver that moves the electrode to precise tissue locations and depths.[30] Recessed-tip microelectrodes (5–10 μm in diameter) were made to reduce tissue damage and microcirculatory disturbance, providing faster responses and finer spatial resolution.[29] Planar electrodes have been designed to allow for transcutaneous oxygen

Table 1: Overview of tissue oxygen sensing techniques.

Technique	Materials	Advantages	Limitations	Specific applications	Ref.
polarographic electrodes	polarographic electrodes	highly quantitative, direct pO_2 measurement, independent of perfusion	invasive, point measurement, location-dependent, consumes oxygen	point measurements, topically or in tissue	[28–30]
imaging of radioisotopes	PET scanner; inhalable or injectable radioactive tracers	3D full-body imaging, non-invasive, scanners available for humans	low spatial resolution, requires short-lived radioactive tracers, relies on perfusion	full-body or organ scanning	[31–33]
resonance imaging	MRT or EPR scanner; injectable contrast agents	non-invasive, tracers are stable or not required	not always quantitative, low spatial resolution	full-body or organ scanning	[33–38]
optical StO_2 measurements	optical systems (e.g., pulse oximeter, DOS/T, PAT, OCT)	non-invasive, portable device, no exogenous contrast agent	measures O_2 saturation instead of pO_2 relies on perfusion, limited sensing depth	clinical monitoring of the O_2 saturation (with pulse oximeter)	[39–45]
phosphorescence quenching	sensor dyes, optical readout devices (e.g., microscope, phosphorimeter, camera)	high spatial resolution, direct quantitative pO_2 measurement	limited light-penetration depth, incapable of full-body imaging	intravascular, interstitial, and intracellular sensing	[46–50]

DOS/T = diffuse optical spectroscopy/tomography, EPR = electron paramagnetic resonance, MR = magnetic resonance, OCT = optical coherence tomography, PAT = photoacoustic tomography, PET = positron emission tomography.

pressure ($TcpO_2$) measurements by attaching the probes on the skin surface.[52] However, the requirement of elevating the skin temperature to 44–45 °C perturbs the examined tissue. These technologies focus on point measurements and have lacked the ability to map oxygen-tension gradients across regions of tissue. Recently, the concept of wearable, bioconformable electronics was introduced by Rogers et al. to overcome this limitation.[53] Patterned silicon integrated-circuit sheets were constructed that are stretchable and cover relatively large tissue areas, paving the way for the development of planar polarographic electrodes that will allow for the two-dimensional mapping of tissue oxygenation. This research direction is highly promising, and future methods should be integratable with existing tissue- and wound-care products.

3. Radioisotope Techniques

In contrast to polarographic methods, which are often invasive and limited to point measurements, radioisotope techniques provide excellent three-dimensional (3D), non-invasive, full-body imaging capabilities. Radioisotope techniques make use of instrumentation capable of imaging the emission of short-lived radioisotopes of elements, such as oxygen, nitrogen, and carbon. These techniques can directly report perfusion changes, oxygen metabolism rates, and the pO_2 levels of healthy and diseased tissues.[34] Radiolabelled agents have been developed for specifically labeling hypoxic tissue regions, such as ^{18}F-fluoromisonidazole (^{18}F-MISO), ^{18}F-fluoroazomycin-arabinoside (^{18}F-FAZA), and ^{18}F-flortanidazole (^{18}F-HX4),[31,32,54] which are based on the selective accumulation of chemically reduced nitroimidazoles in cells experiencing severe hypoxia. Unfortunately, these labeling approaches only show regions of hypoxia and do not provide direct, real-time quantitative measurements of tissue oxygen levels.

3.1. Positron Emission Tomography

Whole-body oxygen imaging can be performed with positron emission tomography (PET), a functional imaging technique that utilizes isotopically labeled chemical species. These isotopes emit positrons, which later interact with electrons, thus generating gamma ray pairs whose detection enables spatial localization with millimeter resolution. PET has been successfully applied for the in vivo monitoring of oxygen supply and consumption by the introduction of ^{15}O-labeled tracers. As ^{15}O has a short half-life of 2.4 min, tracers must be produced on-site using a cyclotron. Steady-state approaches were first introduced in the early 1980s for the non-invasive study of cerebral blood flow and oxygen metabolism in vivo under continuous $^{15}O_2$ gas inhalation.[55,56] Owing to radiation exposure and the difficulty in determining when a steady state is reached, techniques based on short $^{15}O_2$ inhalation followed by dynamic monitoring of ^{15}O were developed and are now in active use.[57]

These methods provide quantitative information on the oxygen supply and consumption in tissue by determining the

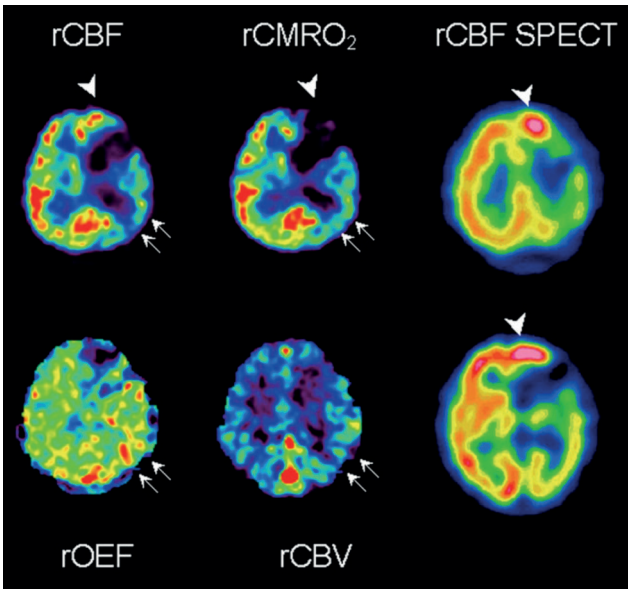

Figure 2. A case of subacute left-hemispheric stroke caused by left internal carotid occlusion. A ^{15}O PET study (left and center column) clearly demonstrates luxury perfusion in the left frontal cortex (arrowhead). SPECT perfusion imaging using ^{99m}Tc-HMPAO (right column) demonstrates hyperperfusion and hyperfixation in the same region (arrowhead). Misery perfusion is also seen in the left temporo-occipital region (small arrows). rCBF = regional cerebral blood flow, rCBV = regional cerebral blood volume, $rCMRO_2$ = regional cerebral metabolic rate of oxygen, rOEF = regional oxygen extraction fraction. Reproduced with permission from Ref. [74].

influx rate of $^{15}O_2$ from arterial blood. Parameters, such as the cerebral blood volume (CBV), cerebral blood flow (CBF), oxygen extraction fraction (OEF), and cerebral metabolic rate of oxygen ($CMRO_2$), can be calculated based on the clearance rate of $^{15}O_2$ (Figure 2). These parameters have been measured for determining the degree of cerebral ischemia in studies of arterial occlusion, stroke,[58] brain tumors,[59] and traumatic brain injuries.[60–64] Furthermore, this technique has been extended to applications in other organs, such as the heart.[65] Proposed clinical indications range from assessing chronic ischemia and tumor stages in cancer[59] to predicting neurological outcomes in patients suffering from acute ischemic stroke.[66]

3.2. Single-Photon Emission Computed Tomography and Combined Techniques

Whereas PET detects the emission of gamma ray pairs following positron–electron annihilation, single-photon emission computed tomography (SPECT) simply relies on individually detected gamma ray photons. Although its intrinsic spatial resolution is lower than that of PET, SPECT images are much simpler, less costly to acquire, and can use a wide range of available gamma-emitting isotopes. Using this technique, for example, the regional cerebral blood flow can be measured following technetium-99m hexamethylpropyleneamine oxime (^{99m}Tc-HMPAO) administration (Figure 2). This has been applied in evaluating the effect of an hyperbaric oxygen therapy in patients showing symptoms of carbon monoxide poisoning, with results demonstrating increased regional CBF following therapy.[67] HMPAO SPECT has also been used to study the patterns of regional CBF in patients with corticobasal degeneration, where decreased HMPAO uptake was found in abnormal cortical regions.[68]

Studying physiological disorders related to perfusion and oxygen-metabolism abnormalities frequently involves a combination of complementary imaging techniques for the determination of multi-parameter information. These combined measurements can be performed with specialized multifunctional equipment, such as SPECT–MRI and PET–MRI instruments. In these combined measurements, MRI is typically used for structural imaging with PET or SPECT providing molecule-specific information. These combined approaches have been advantageous for the measurement of oxygen and oxygen metabolism as abnormal regions within organs can be first identified by the MR contrast and then monitored over time using radioisotope techniques.[69–72] In 1993, Yamauchi et al. performed sequential MRI and PET experiments in studies of patients with Alzheimer's disease.[73] MRI was employed to specifically and quantitatively evaluate the degree of corpus callosum atrophy, which was then correlated with PET measurements of the cerebral cortical oxygen metabolism.

Though highly promising, the clinical translation of radioisotope techniques as a routine procedure for tissue oxygen imaging has been impeded by the complexity of the measurements, the exposure of patients to radiation, a low intrinsic spatial resolution, and the need for the on-site production of certain radioactive tracers. Furthermore, measurements can only be performed within perfused tissue regions, and do not directly provide pO_2 values. Despite these limitations, PET continues to serve as the gold standard in the clinical imaging of brain circulation, and is widely used as a reference to validate other oxygen-sensing techniques.

4. Resonance Techniques

Unlike radioisotope techniques, which require tracers with half-lives of minutes to hours, the resonance techniques discussed in this Section utilize stable contrast agents that can be synthesized and stored up to years before use. Resonance techniques take advantage of the non-invasive nature of the magnetic field, and use radiofrequency or microwave radiation to detect specific chemical species in a biological system based on their distinct resonance frequencies within an applied magnetic field. The magnetic resonance (MR) of both atomic nuclei and electrons has been applied for the sensing of molecular oxygen in tissue. Nuclear resonance techniques have been developed based on ^{19}F and ^{1}H MR. Techniques related to electronic resonance are based on electron paramagnetic resonance (EPR) and dynamic nuclear polarization (DNP).

4.1. Nuclear Resonance Techniques

4.1.1 ^{19}F Magnetic Resonance

In magnetic-resonance imaging, contrast resulting from the spin–lattice relaxation time, T_1, is generated by exciting atomic nuclei with a radiofrequency pulse and then monitoring the rate at which the emitted radiofrequency signal decays as the nuclei return to their original state. The longitudinal component of the magnetization vector returns to equilibrium through spin–lattice relaxation; this process is characterized by the time T_1 and the corresponding relaxation rate R_1 ($= {T_1}^{-1}$).[75] ^{19}F oximetry utilizes perfluorocarbons (PFCs), such as hexafluorobenzene (HFB) and perfluorotributylamine (PFTB), as exogenous contrast agents.[76] As the spin–lattice relaxation rates of ^{19}F in PFCs are linearly dependent on oxygen partial pressure, this method allows access to the whole range of physiological pO_2 values, including hyperbaric conditions.[77] A MR spectroscopic method utilizing PFCs to dynamically monitor tissue pO_2 levels in vivo was developed by Mason et al. in 1991.[78] These principles were later translated into the imaging technique known as FREDOM (fluorocarbon relaxometry using echoplanar imaging for dynamic oxygen mapping).[79]

PFC contrast agents allow oxygen to diffuse more efficiently and are non-toxic. In 1989, Fluosol became the first PFC agent that received FDA approval. Since then, a number of other agents have entered clinical trials, such as Oxygent and Oxycyte. In a typical in vivo ^{19}F MR relaxometry experiment, a PFC is administered intravenously in the form of emulsions or nanoparticles several hours to a few days before the measurement.[78,80] The hydrophobicity of the compounds allows for in vitro calibration curves to be used for in vivo measurements, and also makes them minimally affected by ions and proteins in the blood stream.[81,82] Fluorine nuclear magnetic resonance (NMR) with PFCs typically requires millimolar concentrations of the contrast agents, which are orders of magnitude greater than those of the ^{18}F-based tracers in PET. However, the lack of radioactivity of ^{19}F makes it easy to use, as measurements are not limited by the 110 min half-life associated with ^{18}F-based agents.[76] As particulate PFCs lead to extensive macrophage uptake and sequestration in the reticuloendothelial system, ^{19}F oximetry is particularly efficient in organs such as the liver and spleen.[76]

^{19}F MR oximetry is well established and continues to make important contributions to pre-clinical research. Oxygen measurements have been reported on animal models, including mice,[83] rats,[84] rabbits,[85] cats,[86] and pigs.[87] Long-term studies have been carried out where repeated measurements were performed to monitor tumor oxygen tension over several weeks.[88,89] Recent developments of ^{19}F relaxometry involve the direct local injection of neat PFCs into the tissue of interest to achieve immediate pO_2 imaging.[88,89] ^{19}F MR oximetry has been applied to assess the pharmacodynamic response to interventions that aim at modifying tissue perfusion[90] or oxygen metabolism.[91] Kadayakkara et al. reported the loading of PFCs into cultured stem cells prior to placement in an animal, which allowed for the tracking of stem cell migration and retention in addition to pO_2 measurements.[92] It should be noted that the sensitivity of R_1 to pO_2 is field- and temperature-dependent, and therefore requires the system to be calibrated under experimental conditions. However, the main issue impeding the clinical translation of ^{19}F oximetry remains the lack of clinical MRI scanners that are capable of ^{19}F imaging.[76]

4.1.2 ^{1}H Magnetic Resonance

4.1.2.1 Endogenous Contrast

One of the earliest techniques developed based on endogenous MR contrast is blood oxygen level dependent (BOLD) imaging, which refers to the transverse relaxation time (T_2*)-weighted ^{1}H MR imaging of water using deoxyhemoglobin (dHb) in the venous blood as an endogenous contrast agent.[93,94] The BOLD effect was discovered when high-resolution brain images were acquired from rats using a pulse sequence that accentuated the magnetic-field susceptibility. During the measurement, the contrast from anatomical details of blood vessels was found to reflect the blood oxygen levels. As is now known, this contrast is caused by the difference in the magnetic susceptibilities between oxyhemoglobin (oxyHb) and deoxyhemoglobin; iron(II) has four unpaired electrons in dHb whereas it has none in oxyHb. The inhomogeneities in the local magnetic field caused by the paramagnetic dHb are reflected by changes in the transverse relaxation time T_2* of water in venous blood as well as in tissue surrounding the blood vessels.[35]

Despite being highly advantageous as a non-invasive, exogenous, agent-free technique that generates whole-body images with high temporal and spatial resolution, the application of BOLD for tissue oxygenation measurements is not barrier-free, mainly owing to the lack of direct correlation between T_2* and pO_2.[95] Furthermore, the magnitude of the BOLD effect depends on the total amount of dHb; therefore, changes in the blood volume can counteract the effect of blood oxygenation changes.[38,96] Magnetic-field inhomogeneities that are caused by magnet imperfections, poor shimming, air–tissue interfaces, and metallic implants can also affect the measurements.[35] Moreover, changes in the blood pH value, temperature, and glucose level can alter the hemoglobin dissociation curve, affecting the actual pO_2 value at a given dHb content.[38] Last but not least, for BOLD MRI to be able to provide information on the tissue oxygenation status, it is necessary for red blood cells to be delivered to the tissue in question, which is not the case in many tissues under ischemic or chronically hypoxic conditions, such as tumors with malformed vasculatures.[95]

Human cerebral blood oxygenation has been widely studied with BOLD-MRI.[35,97] Owing to its sensitivity in detecting pO_2 fluctuations, BOLD signals have become the basis of functional MRI (fMRI), which is widely used in the field of cognitive neuroscience. By connecting the BOLD MRI signal to brain hemodynamics and metabolism, the oxygen extraction fraction (OEF) and the cerebral metabolic rate of oxygen consumption ($CMRO_2$) can be determined.[98,99] The technique has also been applied to the monitoring of tumor microenvironments,[100,101] and has been

shown to be most sensitive to oxygen levels adjacent to perfused vessels.[95]

Aside from T_2*, other types of contrast have also been used for MR oximetry. Recently developed tissue oxygen level dependent (TOLD) imaging is based on contrast arising from oxygen-dependent T_1 values. Matsumoto et al. demonstrated the T_1 signals in tumors to be responsive to hyperbaric treatment.[102] Oxygen supply is highly dependent on vascular flow, which can be detected by quantitative T_1 and T_2 measurements and diffusion MRI. These parameters have been shown to be potential markers for tissue hypoxia.[103] Ongoing investigations in human subjects involve the construction of multiparametric maps using endogenous contrast agents for the evaluation of tumor oxygenation.[104]

4.1.2.2. *Exogenous Contrast*

The proton equivalent of ^{19}F relaxometry, ^{1}H oximetry, was developed in the past decade and makes use of commonly available proton MRI scanners. The Mason group developed the PISTOL approach (PISTOL = proton imaging of siloxanes to map tissue oxygenation levels),[105] which uses siloxanes as contrast agents and functions based on the linear relationship between the spin–lattice relaxation rate R_1 ($= T_1^{-1}$) of protons in siloxane and the local pO_2 value. The most commonly used siloxane is hexamethyldisiloxane (HMDSO), although similar compounds have also been investigated.[106,107] HMDSO was chosen as an optimal PISTOL contrast agent largely owing to its similarity to the known HFB, which is used in ^{19}F relaxometry. The molecular symmetry of the siloxane and the lower electronegativity of silicon provide a single NMR signal that is spectrally well separated from those arising from tissue. This allows HMDSO to be easily identified while suppressing signals arising from water and fat. HMDSO exhibits a dynamic range capable of sensing physiological oxygen levels at body temperatures, and has been reported to be inert and non-toxic.[108]

This technique has also been applied to monitor tissue oxygenation in rodent models. Using a spectroscopic imaging approach, Gulaka et al. reported the measurement of pO_2 values in thigh muscles of Fisher 344 rats in response to oxygen challenge tests (Figure 3).[106] Limitations of the technique mainly arise from the use of exogenous contrast agents, the variance caused by the clearance of these agents, the need for repeated injections for long-term monitoring, and undesired biodistributions of the contrast agent. Recent developments in PISTOL have focused on the design of optimal delivery vehicles for siloxanes. For example, Liu et al. recently demonstrated that embedded contrast agents chemically directed to target organs can achieve longer retention times for longitudinal tissue oxygenation monitoring.[107]

4.2. *Electron Resonance Techniques*

A magnetic resonance technique for probing the resonance of unpaired electrons, electron paramagnetic resonance (EPR), is capable of detecting paramagnetic chemical species, including triplet-state molecules and radicals. As a natural ground-state triplet molecule, molecular oxygen is inherently paramagnetic, but the direct detection of oxygen in biological systems is not possible owing to the broadening of its spectral lines.[38] Therefore, sensing oxygen by EPR requires exogenous paramagnetic substances.[109] As the in vivo levels of other endogenous paramagnetic species, such as metal ions and free radicals, are generally too low to generate interfering background EPR signals, exogenous EPR contrast agents can provide high sensitivity and high signal-to-noise ratios for oxygen sensing. However, the biocompatibility of such EPR agents must be carefully considered. Two classes of paramagnetic materials are most commonly used for EPR oximetry: soluble materials (e.g., nitroxides, triaryl methyl radicals) and insoluble particulate materials (e.g., lithium phthalocyanine, coals, chars, inks, and carbon blacks).[38]

Nitroxides are either administered alone or linked to carrier molecules to achieve tissue and cellular selectivity. They have the disadvantage of being unstable in the biological milieu and are quickly converted into diamagnetic hydroxylamines. Advantageously, this metabolic process is oxygen-dependent and therefore can be utilized to monitor redox states both in vitro and in vivo.[109] The development of particulate paramagnetic contrast agents had a strong impact on the in vivo applications of EPR oximetry. Compared to soluble free radicals, insoluble particulate paramagnetic materials have much higher spin densities that provide, in some cases, up to 1000-fold greater sensitivities for oxygen.[36] These materials are also stable across a wide range of pH values and redox conditions, enabling repeated measurements of the pO_2 value at the same site. The first EPR oximetry experiments in humans were carried out using India inks, which are suspensions of carbon black particles first discovered thousands of years ago in China during the Neolithic period.[36]

EPR oximetry has been used to measure oxygenation in the murine brain,[101,110] heart,[111] gastrointestinal tract,[112]

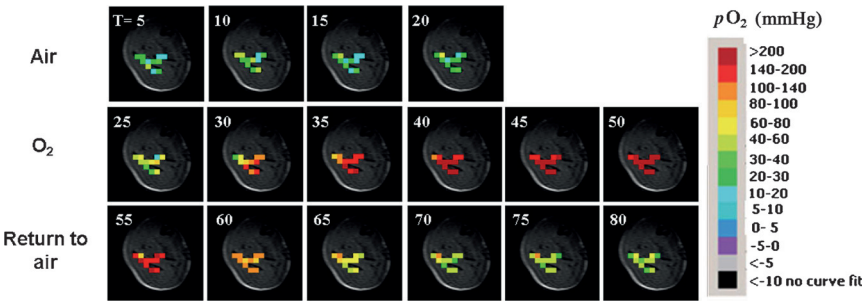

Figure 3. Mapping changes in oxygenation in vivo with respect to oxygen challenge using HMDSO nanoprobes. Spin-echo image of a representative Fisher 344 rat thigh muscle overlaid with time-course PISTOL pO_2 maps (top: baseline air breathing for 20 min; middle: 30 min of oxygen breathing; bottom: 30 min of return to air breathing), showing the response to hyperoxic gas intervention. The acquisition for the first pO_2 map started at $t = 1.5$ min, and the end time (in min) is displayed on the images. Reproduced with permission from Ref. [106].

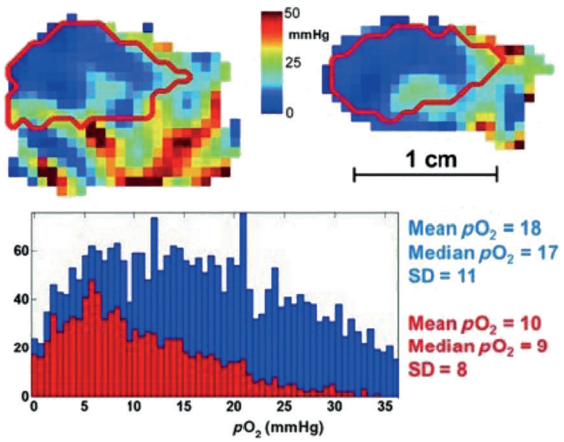

Figure 4. An EPR oxygen image of a murine leg with a MCa4 tumor. Sagittal (left) and coronal (right) slices are presented, with the tumor outline obtained from MRI (red). The color bar shows the pO_2 scale in the range of 0–50 mmHg. The histogram shows pO_2 values from the whole image (blue) and from the tumor volume only (red). The maximum pO_2 values were found to be as high as 50 mmHg in approximately 10 voxels in the leg and 35 mmHg in single voxels in the tumor. Reproduced with permission from Ref. [118].

skeletal muscle,[113] liver,[114] kidneys,[115] and skin,[116] as well as in pathophysiological conditions such as cancer.[101,117] It has a high sensitivity at low pO_2 values, and repetitive measurements can be carried out at the same site for long-term tissue monitoring (Figure 4).[118,119] It has also been used to monitor tumor oxygenation following photodynamic therapy, revealing time-dependent pO_2 changes that are due to vascular shutdown.[120] However, for EPR oximetry to move forward to the clinic, the biocompatibility of the particulate oxygen sensors must be more thoroughly tested. Early clinical studies have only made use of either existing carbon-black-based tattoos, the application of paramagnetic materials on the surface of the skin, or the injection of India ink into specific sites.[36] Moreover, for oxygen-sensing applications, instruments operating at low frequency (<300 MHz) need to be developed to increase the imaging depth to scales suitable for human applications beneath the skin.

As an alternative to EPR, dynamic nuclear polarization (DNP) detects free radicals in biological samples by collecting NMR images while irradiating specific EPR resonances. The transfer of polarization from the electrons to the protons results in an amplification of the observed NMR signal by the Overhauser effect.[121] It was found that the Overhauser enhancement factor is dependent on the linewidth of the paramagnetic compound and therefore inversely proportional to pO_2.[122] Krishna et al. demonstrated this principle in a murine tumor model using Oxo63,[121] a trityl radical, to obtain oxygenation images. When the EPR was "on", the T_2 contrast at tumor regions was significantly enhanced owing to the accumulation of Oxo63, and changes in pO_2 in response to carbogen inhalation tests were demonstrated.

Nuclear medicine and resonance techniques developed in the past few decades have enabled the non-invasive 3D full-body imaging of a variety of physiologically relevant parameters, and have significantly improved our understanding of oxygen distribution on the level of tissues and organs (Table 2).[33,34,38] With millimeter to centimeter voxel sizes, these techniques are largely limited in their capabilities to resolve microscopic tissue information. For instance, MR techniques are excellent for locating macroscopic tumor mass during a full-body scan, but do not provide information on tumor heterogeneity in submillimeter lesions. Furthermore, resonance techniques are not suitable for topical applications owing to the signal interference at the tissue–air interface, and therefore cannot be readily used to assess wound oxygenation and healing potentials. These techniques also rely on advanced instruments that are large and expensive, which renders their use difficult in a number of clinical and field scenarios. Tissue oxygen sensing based on optical measurements in many ways complements the above described methods by providing microscopic resolution and uses readout devices that can be made highly portable for bedside use.

5. Optical Methods for the Hemoglobin-Based Assessment of Oxygen Saturation

The majority of optical methods for measuring oxygen are based on two fundamental approaches: the absorption contrast from hemoglobin–oxygen binding and luminescence quenching by oxygen. Although these two methods both

Table 2: Resonance methods for measuring oxygen in tissue.

	Method	Contrast agent/type	Features	Limitations	Ref.
nuclear resonance	^{19}F relaxometry	perfluorocarbons (PFCs)/T_1	high sensitivity, no tissue background signal	lack of ^{19}F-capable clinical MRI scanners	[37, 75–92]
	BOLD/TOLD	endogenous dHb/T_2* or T_1	non-invasive, no need for injecting a contrast agent	not directly quantitative	[35, 38, 93–104]
	^{1}H relaxometry	siloxanes/T_1	can be performed on proton MRI scanners	advanced contrast agents needed	[105–108]
electron resonance	ESR	paramagnetic materials/ T_2-related	more sensitive to oxygen than NMR at low pO_2	lack of clinical EPR scanners for humans	[36, 38, 109–120]
	dynamic nuclear polarization	paramagnetic radicals/ EPR-enhanced NMR	NMR signals enhanced owing to electron resonance	requires instruments with low field irradiation	[121, 122]

measure the oxygen content, each approach reports important, but different metrics of oxygenation. Absorption-contrast methods utilize the fact that oxyhemoglobin and deoxyhemoglobin have different absorption spectra to calculate oxygen saturation (StO_2); luminescence-based methods, which rely on emission quenching through collisions with molecular oxygen, instead directly report absolute oxygen concentration.

StO_2 is an important clinical metric of blood oxygenation that can be detected by multiple absorption methods, including pulse oximetry,[39] diffuse optical spectroscopy and tomography,[123,124] photoacoustic tomography,[42] and optical coherence tomography.[125] As the absorption contrast of hemoglobin does not require the addition of dyes or labels, these methods are of high clinical utility. The most familiar of these tools, the pulse oximeter, works by transmitting and detecting the differential absorption of two wavelengths of light, typically 660 and 940 nm, through thin tissues, such as a fingertip or earlobe; 660 nm light experiences greater absorption by deoxyhemoglobin whereas 940 nm light is more strongly absorbed by oxyhemoglobin. By measuring the periodic modulation of this differential absorption that is due to pulsed blood flow, pulse oximetry isolates the oxygen saturation of arterial blood alone without contributions from other absorbing species, such as venous blood. Details on the development of pulse oximetry and its many applications can be found in several excellent reviews.[39,126,127]

Diffuse optical spectroscopy and tomography (DOS/T) also provide absorption-based contrasts, including StO_2 values, but are more complex and offer considerably greater utility. In DOS/T, light of different wavelengths is launched into tissue, where it is then absorbed or scattered within the turbid tissue environment. Some of the scattered photons can be redirected towards detectors; depending on the type of DOS/T system, the detectors can be set up either in trans-illumination or reflection modes. The spectrum of the scattered photons that arrive at each detector can be measured at different distances and positions from the light source, revealing the absorption of light at both specific locations and depths within tissue. By employing arrays of emitters and detectors, DOT can generate 3D tomograms of tissue parameters, including oxygen saturation.[128] Transillumination mode configurations have been found useful for measuring StO_2 in breast cancer.[129] One of the most prominent applications of DOT was in the noninvasive measurement of brain oxygenation led by Chance. In a series of studies, Chance and co-workers were able to measure not only static StO_2 values,[124] but also dynamic changes caused by mental activity in different regions of the brain. Comprehensive review articles are available on the development and applications of diffuse optical spectroscopy, tomography, and imaging.[40,41,130]

The absorption of light by hemoglobin can also be directly detected by taking advantage of photothermal effects. When a molecule absorbs light, the energy can be redistributed into the environment through localized heating. If photons are delivered in a short burst, the thermal deposition can cause the molecules' surroundings to rapidly expand in volume, creating an ultrasonic wave that can be detected. This is the principle underlying the recently developed photoacoustic tomography (PAT), which can visualize the three-dimensional position of molecules in tissue by absorption contrast. PAT excels at the measurement of hemoglobin oxygen saturation through differential absorption measurements similar to those used in pulse oximetry and DOS. As the contrast is generated optically but sensed via ultrasound, PAT offers high-resolution, millimeter-deep imaging of the vasculature in tissue.[42,43]

Optical coherence tomography (OCT) is an optical ranging technology analogous to ultrasound: Using low-coherence interferometry, OCT is capable of rapidly creating high-resolution (<1 μm) tomograms of tissue with millimeters of optical penetration. Spectral-domain OCT (SD-OCT) makes use of broadband near-infrared light and spectral detectors, such that it is possible to use the absorption information encoded in the spectral interferogram to glean information on the oxygen saturation from a tissue. This approach, named spectroscopic OCT, is still in development and shows promise in detecting the blood oxygenation status.[45,131] Taking advantage of the same photothermal effects that are used for photoacoustic imaging, photothermal OCT methods have recently been developed. By alternating the exposure of tissue to two frequencies of near-infrared light, dual-wavelength photothermal OCT can selectively detect the hemoglobin-absorption-induced phase change of blood to calculate the oxygen saturation at depths in tissue in vivo.[44,132]

6. Oxygen Sensing Based on Luminescence Quenching

StO_2 sensing, while a useful approach towards measuring the oxygen contained in blood, relies on the existence of perfusion and does not reveal information regarding the concentration of dissolved oxygen within tissues and cells themselves. Knowledge of tissue oxygen tension is critical in the detection and study of hypoxia and ischemia, which can occur even in regions seemingly well fed by blood vessels with high StO_2. Optical-imaging approaches based on luminescence quenching enable the direct measurement and quantification of oxygen concentrations within tissues, even in the absence of blood. As luminescent sensors are a topic of intense study in the fields of chemistry, biophysics, and medicine, the remainder of this Section will focus on recent developments of luminescence-quenching methods.

For a comprehensive background, readers are recommended a number of detailed recent review articles that have presented the many materials developed for optical oxygen sensing, their design principles, measurement techniques, and applications.[46–50]

Optical oxygen sensors based on luminescence quenching operate through energy exchange, where excited-state luminophores transfer energy to surrounding molecular oxygen and thereby no longer emit. The quenching effect on the luminescence intensity and lifetime of a sensor is described by the Stern–Volmer equation [Eq. (1)]:

$$\frac{I_0}{I} = \frac{\tau_0}{\tau} = 1 + k_q \tau_0 p O_2 \quad (1)$$

where I_0 and τ_0 are the phosphorescence intensity and lifetime, respectively, in the absence of oxygen. I and τ are the corresponding parameters at a given oxygen partial pressure pO_2, and k_q is the quenching constant related to the diffusion rate of oxygen and the luminophore.[133] Both intensity and lifetime measurements have been realized on systems spanning spectrometers, cameras, and microscopes, providing measurement capabilities on different spatial and temporal scales.[50]

Luminescence-intensity-based approaches are advantageous in their simplicity, and can be easily adapted to existing imaging systems. For example, commercially available CCD and CMOS cameras have been used to capture the distribution of phosphorescence intensity and quantify oxygen across two-dimensional surfaces.[133,134] Although the method can be limited by inhomogeneous illumination and a non-uniform distribution of the probe molecules, these challenges can be overcome by introducing an oxygen-independent reference dye that co-localizes with the phosphorescent sensor. Digital color cameras that use separate RGB channels have been applied to measure the ratio of these signals.[135] High-resolution intensity-based oxygen imaging on the cellular and subcellular levels has also been achieved using laser-scanning microscopes.[136]

In contrast, lifetime-based approaches are advantageously independent of excitation intensity, detector sensitivity, and probe concentration, and have been realized by either time- or frequency-domain methods. Time-domain measurements involve exciting the probe molecules with a temporally short light pulse and then recording the decay profile, typically using methods such as time-correlated single-photon counting. The rapid lifetime determination method introduced by Woods et al.[137] allowed the calculation of phosphorescence lifetimes using the intensities captured at two separate time windows along the decay curve. Lifetime-based imaging has also been performed with time-gated CCD cameras.[48,138–140] Frequency-domain measurements, on the other hand, involve exciting probe molecules with modulated light, with lifetimes determined by measuring the phase shift between the excitation and emission signals.[141,142] When long-lifetime (>1 μs) probes are used, gated acquisition allows for the effective suppression of background fluorescence.[143]

These methods have enabled a host of studies involving measurement of intravascular pO_2 values in various tissue types, including tumors, the brain, retina, and heart.[144–147] Aside from the most commonly deployed intensity- and lifetime-based oxygen readout systems, many other approaches, such as fluorescence anisotropy measurements,[148] Förster resonance energy transfer (FRET),[149] and two-photon excitation[7,147,150] techniques, have also been adapted for oxygen-sensing purposes, each adding their unique features for specific application needs.

6.1. Probe Design

The introduction of the oxygen-dependent quenching of phosphorescence[133,134] led to a boost in the design and synthesis of oxygen sensors. To transition from the simple ruthenium(II) and iridium(II) complexes that were used in early studies, synthetic chemistry principles were implemented to develop more advanced porpyrin-based probes with highly tunable structural and spectral properties that are suitable for use in biological environments.

6.1.1. Ruthenium(II) and Iridium(II) Complexes

Early applications of physiological oxygen sensing involved the use of simple complexes that were either commercially available or could be prepared by following straightforward procedures. Ruthenium complexes, such as $[Ru(bpy)_3]^{2+}$ (bpy = 2,2′-bipyridine)[151–153] and $[Ru(phen)_3]^{2+}$ (phen = 1,10-phenanthroline),[152,154] have been used to image intracellular oxygen in murine and human cell lines (Table 3). Their limitations included poor membrane permeability and intracellular distribution heterogeneities. The latter challenges can be overcome by lifetime-imaging approaches.[151,153] Improved cellular uptake has been achieved by modifying the ruthenium ligands. [Ru(bpy-pyr)-$(bpy)_2$] (bpy-pyr = 4-(1″-pyrenyl)-2,2′-bipyridine)[155] and [Ru-Py] ($[(bpy)_2Ru(N$-(pyren-1-ylmethyl)-1,10-phenanthrolin-5-amine)$]^{2+}Cl^-_2$; Py = N-(pyren-1-ylmethyl)-1,10-phenanthrolin-5-amine),[156] both bearing lipophilic substituents on the ligands, exhibited enhanced cell-membrane permeability as well as a response to changes in intracellular oxygen levels. [Ru-Py] was also found to be effective in detecting ischemia in the leg of nude mice that was due to the reduced blood flow caused by a ligature.[156]

Compared to ruthenium complexes, iridium sensors offer a broader color-tuning potential, enabling the synthesis of probes emitting in the near-infrared (NIR) region for deep-tissue oxygen sensing (Table 3).[157] At NIR wavelengths, light penetration is higher than at visible wavelengths, as NIR light is significantly less scattered in turbid tissue. The synthetic tunability offered by the acetylacetonate ligand in the BTP complex ([Ir(btp)$_2$(acac)], bis(2-(2′-benzothienyl)pyridinato-N,C$^{3'}$)iridium(acetylacetonate)), an iridium complex that has been used in visualizing subcutaneous tumor oxygenation in nude mice,[158] has been exploited to create functionalized oxygen probes. BTPHSA, a carboxylic acid derivative of BTP designed to absorb and phosphoresce at longer wavelengths, allowed the visualization of tumors at greater depths than BTP, enabling whole-animal oxygen imaging at a depth of several millimeters.[158] Functionalization of the acetylacetonate ligand on BTP with a triphenylphosphonium cation resulted in BTP-Mito, the first mitochondria-specific oxygen-sensing iridium complex.[159] Yoshihara et al. recently reported C343-Pro4-BTP,[149] a ratiometric, FRET-excitable sensor that comprises a covalent conjugate of BTP and Coumarin 343 (C343) linked via a linear proline tetramer. The probe displayed oxygen-dependent phosphorescence emission inside living HeLa cells (Figure 5).

Table 3: Luminescent oxygen-sensing Ru^{II} and Ir^{II} complexes and their applications.

Probe	Experimental system	Comments	Ref.
$[Ru(bpy)_3]^{2+}$	J774 macrophages	lifetime imaging, non-uniform intensity, constant lifetime	[151]
	human fibroblasts	no penetration through intact membranes	[152]
	BEAS-$2B_{NNK}$ epithelial cells	lifetime measurements, independent of concentration	[153]
$[Ru(phen)_3]^{2+}$	J144 macrophages	high concentration and long incubation required	[152]
	J774 macrophages	high concentration required	[154]
$[Ru(bpy\text{-}pyr)(bpy)_2]$	J774 macrophages	passive membrane penetration	[155]
[Ru-Py]	human lung adenocarcinoma (A549) cells	enhanced cell permeability, in vivo ischemia imaging	[156]
BTP	mouse oral squamous carcinoma derived SCC-7 cells	subcutaneous tumor oxygenation in vivo	[158]
BTPHSA	SCC-7 cells	NIR emitting, in vivo imaging at greater depths	[158]
C343-Pro_4-BTP	HeLa cells	limited uptake, FRET excitable, ratiometric	[149]

6.1.2. *Porphyrin-Based Sensors*

Although Ru and Ir complexes have been useful as substrates for building derivatized oxygen sensors, there is a limitation on the number and type of ligands that the central metal can accommodate. The metalloporphyrin classes that were developed over the past few decades, on the other hand, contain a variety of peripheral groups that can be readily functionalized. Furthermore, platinum and palladium porphyrins have superior photophysical properties for oxygen-sensing applications, such as significantly higher room-temperature phosphorescence quantum yields and longer lifetimes than Ru and Ir sensors.

Unmodified platinum and palladium porphyrin complexes were successful in early studies that made use of the phosphorescence quenching techniques to identify physiological oxygen variations in tissues under different conditions. The Wilson group measured oxygen distributions ex vivo in isolated rat livers, which were perfused through the portal vein with a palladium/coproporphyrin-containing medium.[133] Palladium meso-tetra(4-carboxyphenyl)porphine (PdTCPP) has been utilized for the measurement of oxygen pressure distributions in the brain of anesthetized animals during experimentally induced hypoxia and reperfusion,[160] and the acquisition of pO_2 maps in the retinas of animal models.[146,161] A microscope-based imaging system that was developed by Shonat and Kight[146] to perform phosphorescence lifetime measurements used the PdTCPP probe by injection into the retinal and choroidal vessels of mice. Oxygen tension maps created at different systemic oxygen levels showed differences

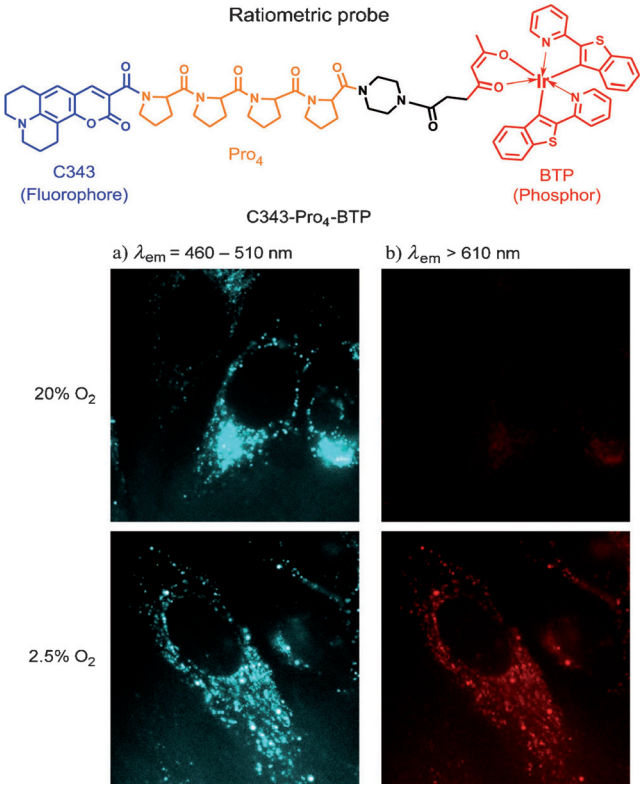

Figure 5. Top: Structure of the ratiometric sensor C343-Pro4-BTP. Bottom: Luminescence images (λ_{ex} = 400–410 nm) of HeLa cells incubated under 20% and 2.5% O_2 and imaged at λ_{em} = 460–510 nm (a) and above 610 nm (b). Adapted with permission from Ref. [149].

between the arterial, venous, and capillary regions of the retina (Figure 6).

Synthetically extending the π structure of the Pt and Pd porphyrins results in a red shift in their absorption spectra. The resulting probes, which absorb in the red and NIR region, allow for deeper light penetration and improved imaging depth. Green 2W, a water-soluble analogue of palladium meso-tetraphenyltetrabenzoporphyrin (PdTBP), enabled the non-invasive in vivo imaging of pO_2 in the vasculature of mice bearing subcutaneous tumors.[162] Furthermore, oxygen-sensing porphyrins with red and NIR emission and longer lifetimes are easily distinguishable from fluorophores and can be used for the development of dual-imaging approaches. For example, a fluorescence/phosphorescence system was developed by Barlow et al. to combine NADH fluorescence imaging with oxygen concentration monitoring,[163] utilizing Pd^{II} meso-tetra(*para*-sulfonatophenyl)porphyrin (PdTSPP) as the oxygen sensor.

Despite the success of these early unmodified metalloporphyrins in intravascular pO_2 sensing, the application of most of these sensors is limited by their low solubility in aqueous media and their high degree of interactions with the macromolecules present in biological environments. To overcome these challenges, porphyrin molecules have been synthesized with multiple surface functional groups to enable the construction of dendrimers and macromolecular sensors (summarized in Table 4). These constructs can have improved solubilities and biocompatibilities over "naked" porphyrins, and can be combined with targeting moieties for improved biodistribution.

Among the first oxygen-sensing porphyrin dendrimers reported were Oxyphors R2 and G2, two water-soluble, second-generation polyglutamic palladium porphyrin dendrimers with PdTCPP and PdTBP cores, respectively.[164–166] The calibration constants of these early intravascular probes were found to be well suited for measurements of physiological oxygen tensions owing to their albumin binding. They have been used for the measurement of oxygen pressures in animal tissues[167–169] and subcutaneous tumors.[142,145,166] The advantages, design, and properties of porphyrin cores encapsulated inside dendritic layers have been extensively discussed in a book chapter by Vinogradov and Wilson.[48] More

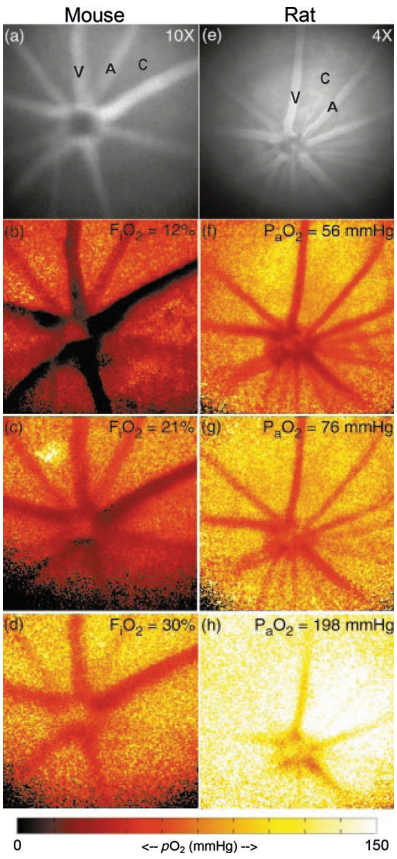

Figure 6. Phosphorescence intensity images (a and e) and colorized 2D maps of one mouse and one rat retina. The maps indicate inspiratory oxygen fractions (F_iO_2) and arterial blood-gas oxygen tension (PaO_2) for the mouse and the rat, respectively. The upper right corners of images (a) and (e) show the microscope objectives used. Arterial (A), venous (V), and capillary (C) regions are indicated on images (a) and (e). Reproduced with permission from Ref. [146].

Table 4: Oxygen-sensing porphyrin dendrimers and their applications.

Probe	Application	Comments	Ref.
Oxyphor R2	animal tissues		[167–169]
Oxyphor G2	subcutaneous tumors	NIR-excitable, increased imaging depth	[142,145,166]
Oxyphor G3	pO_2 in skeletal muscles,		[170]
	interstitial pO_2 in tumors,	NIR-excitable,	[171]
	myocardial oxygenation	PEG-coated, unaffected by albumin	[172]
Oxyphor G4	tissue oxygenation in tumor-bearing mice		[173]
G3-CAOS	ovarian-cancer monolayer cultures and multicellular 3D spheroids	NIR-excitable, polycationic and cell-permeable	[136]
PtP-C343	in vivo pO_2 maps in cerebral vasculature and bone marrow	two-photon excitable, FRET-activated	[7,147,150,176–179]
PtTCHP-C307		two-photon excitable, increased FRET efficiency	[180]

recent advancements have been made in the development of phosphors that could function independently of the presence of albumin. This was achieved with the addition of a surface poly(ethylene glycol) (PEG) layer. Among the probes synthesized and evaluated in in vivo studies of tissue oxygenation are Oxyphor G3[170–172] as well as Oxyphors R4 and G4.[173]

The porphyrin dendrimers discussed thus far have been designed for intravascular oxygenation imaging studies and lack the ability to penetrate cellular membranes. Motivated by the need to enhance cell penetration for delivering oxygen sensors through multiple cellular layers into solid tissue, Nichols et al. recently developed a cell-permeable polycationic porphyrin dendrimer consisting of an azido-functionalized analogue of PtTBP surrounded by poly(amidoamine) (PAMAM) like dendritic subunits (Figure 7).[136] To build the dendron subunits, a sequential synthetic scheme was designed that enabled their rapid assembly by click chemistry. Near-infrared confocal phosphorescence microscopy demonstrated the ability of the new sensor, the G3-CAOS (click-assembled oxygen sensing) probe, to penetrate hundreds of micrometers into multicellular spheroids, and showed its sensitivity to induced oxygen changes (Figure 7). To the best of our knowledge, this is the first oxygen-sensing porphyrin dendrimer that spontaneously penetrates not only monolayer cell membranes but also multiple cell layers without facilitated uptake or the need for delivery vesicles or cell-penetrating peptides.

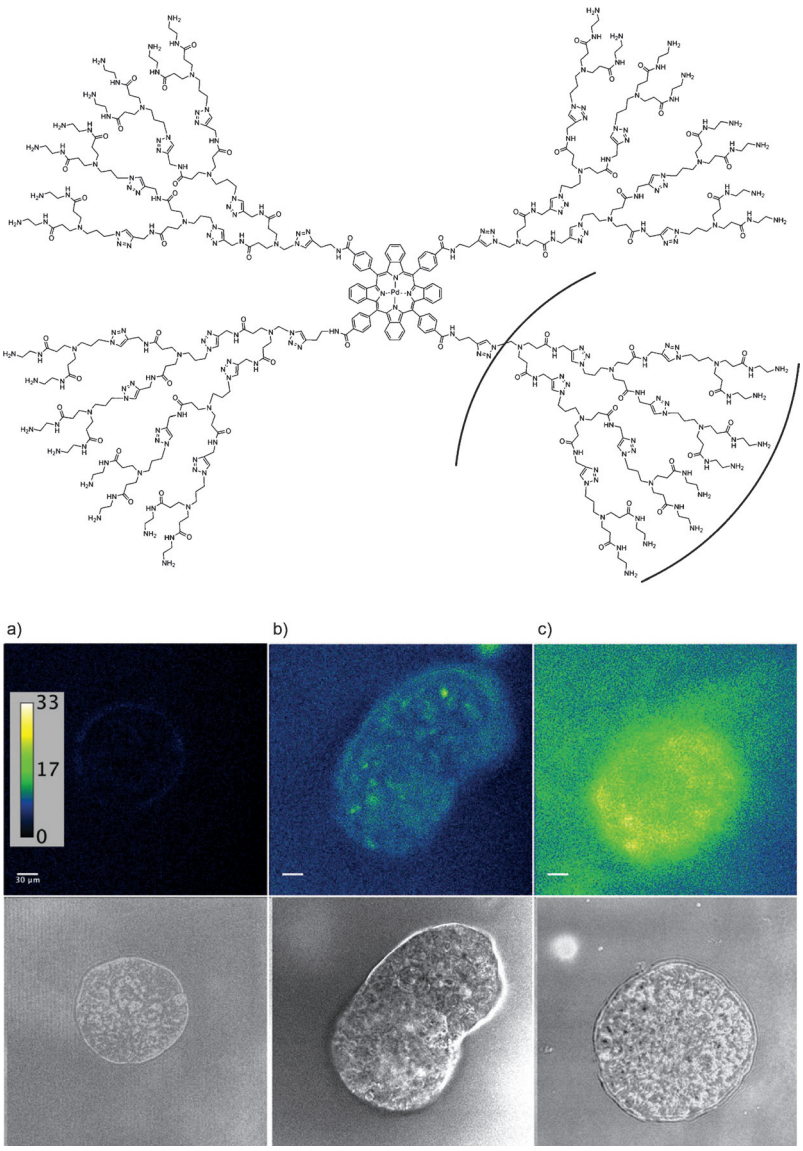

Figure 7. Top: Structure of the G3 CAOS sensor. Bottom: Panels showing phosphorescence confocal microscopy images of 3D ovarian cancer spheroids (bottom row: transmission channel). a) Untreated control. b,c) Spheroids treated for 4 h with 2 µM G3 CAOS imaged under air (b) or after a N_2 purge (c). The color scale bar in (a) represents the number of photons collected. Adapted from Ref. [136].

Another long-standing challenge faced by luminescent oxygen sensors is the inherent depth limitation of visible-light excitation. To achieve deep pO_2 imaging, the Vinogradov group pioneered the design and development of a new class of dendritic probes that combined the phosphorescence quenching technique with two-photon microscopy,[174–177] which utilizes NIR light for excitation and greatly improves the imaging depth without sacrificing image resolution. These new probes contained dendritic surfaces decorated with two-photon-absorbing chromophores that were coated with an additional PEG layer. Two-photon excitation within the layer of antenna chromophores could be transferred to the central porphyrin by FRET. The first two-photon probe that was synthesized, PtP-C343,[176] has been used in combination with two-photon phosphorescence lifetime microscopy in in vivo studies that enabled the first non-invasive 3D measurements of the oxygen distribution in regions of the cerebrum[147,150,178,179] and bone marrow[7] in live animals with high temporal and spatial resolution. Recently, the development of a new two-photon antenna–core oxygen probe, PtTCHP-C307, was reported, which was designed to display enhanced features, such as a significantly increased phosphorescence quantum yield, higher FRET efficiencies because of minimized quenching by electron transfer, and an increased signal dynamic range.[180] PtTCHP-C307 was evaluated in an in vivo measurement of intravascular pO_2 in the bone marrow of a live mouse through the intact skull (Figure 8). The result was fully in line with recent observations using PtP-C343.[7] The dynamic range of the lifetimes of the new probe was found to be optimal for pO_2 measurements under most physiological conditions (0–60 mmHg), although it is strongly quenched at higher oxygen levels.

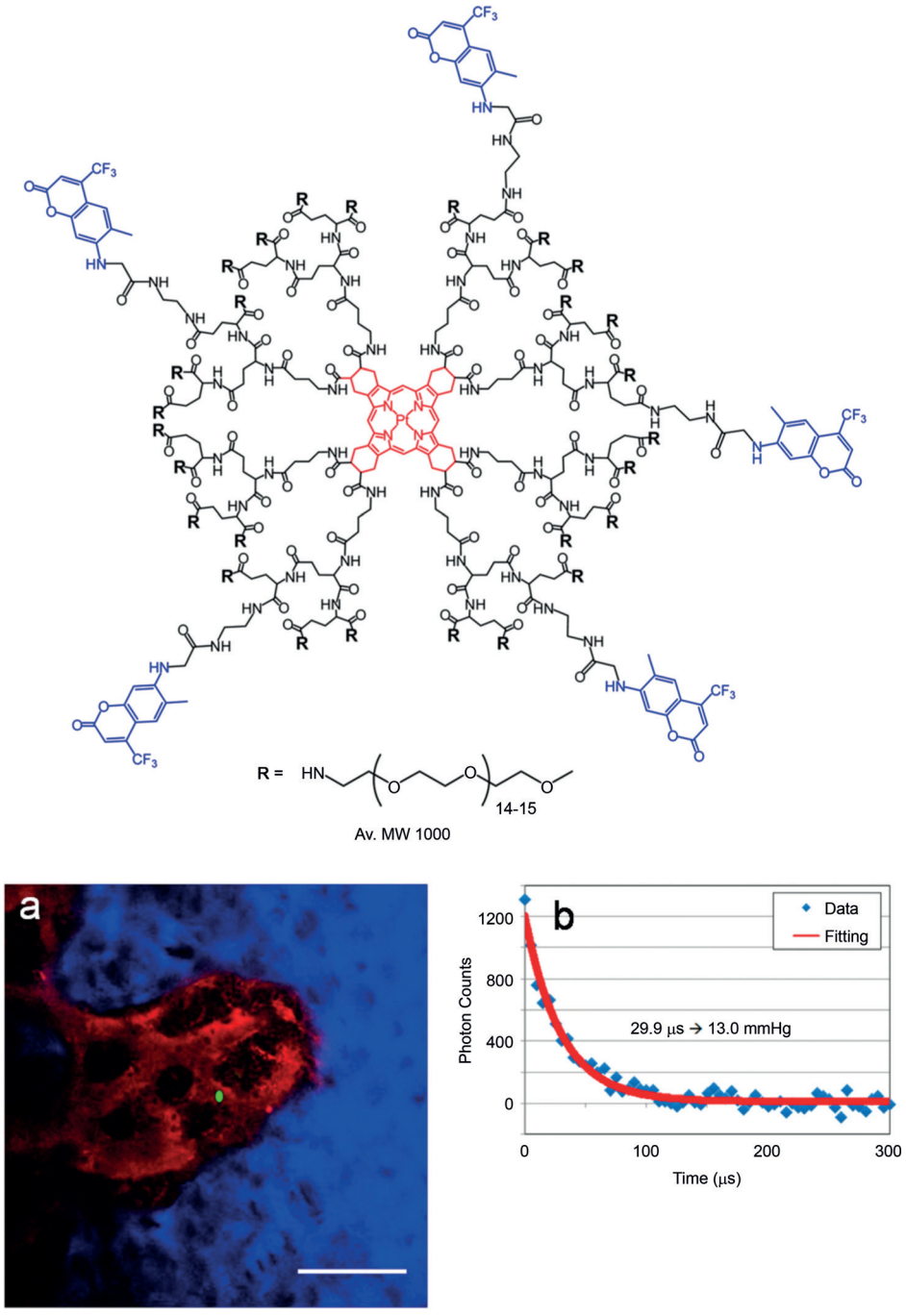

Figure 8. Top: Structure of PtTCHP-C307. Bottom: a) Image of the bone-marrow vasculature showing the point of phosphorescence lifetime measurements as a green dot. The blue contrast arises from second harmonic generations from the bone, whereas the red contrast is due to rhodamine-dextran circulating in the vasculature. b) Data fitting with a single exponential function gave a pO_2 value of 13 mmHg. Scale bar: 100 µm. Adapted from Ref. [180].

6.2. Formulations and Delivery

The use of "bare" porphyrin cores as stand-alone molecular sensors has been hampered by their poor solubility, inefficient cell-membrane permeability, and nontrivial interactions with biomolecules. Beyond the special endogenous generation methods developed by Mik et al.,[181–183] there are a limited number of approaches that provide reliable sensor delivery. Whereas dendrimers offer one potential route, probe research efforts have also been focused on developing conjugates of small-molecule oxygen sensors with macromolecular carriers or cell-penetrating peptides. The encapsulation of oxygen-sensing molecules within nanomaterials has also been an active research area, overcoming some of the limitations associated with the use of the cell-penetrating conjugates. Oxygen-sensing films and foils have additionally been developed as a non-invasive technology, where materials applied on tissue surfaces can be used for the monitoring of oxygenation.

6.2.1. Delivery Methods Based on Conjugates

Conjugation with macromolecular carriers, such as bovine serum albumin (BSA) or PEG, can help increase the hemocompatibility of the porphyrin probes. A panel of oxygen-sensing conjugates was reported by the group of Papkovsky,[184,185] consisting of commonly used porphyrins and BSA or PEG. Platinum coproporphyrin BSA (PtCP-BSA) and PtCP-PEG conjugates were used to monitor oxygen uptake in *E. coli* bacteria cells. The covalent conjugates of PtCP, platinum coproporphyrin ketone (PtCPK) and palladium coproporphyrin ketone (PdCPK) with BSA,[186] also enabled measurements of the transient changes in intracellular oxygen levels in A549, Jurkat, and HeLa cell lines. The study of these probes showed that in some cases, particularly in cell lines of mammalian origin, intracellular delivery of macromolecular conjugates required techniques involving transfection reagents.[186]

The logical next step for improving delivery was the design of oxygen probes attached to cell-penetrating peptides, such as the TAT sequence, which has been known to enhance cellular uptake without the need for transfection reagents or other means of facilitated uptake. This class of oxygen sensors has utilized a range of porphyrins and peptides,[187,188] such as mono- or tetrasubstituted PtCP derivatives with arginine-rich

peptides,[189] iridium octaethylporphyrin (Ir-OEP) covalently linked to different oligopeptides,[190] and platinum tetrakis-(pentafluorophenyl)porphine (PtPFPP) conjugated to monosaccharide and short amino-acid carriers.[191] The last group of small-molecule sensors achieved high-resolution 3D oxygenation mapping in multi-cellular spheroid cultures and brain-tissue slices. Although the majority of intracellular oxygen sensors are based on metallated porphyrins, ruthenium complexes have also been utilized.[192] The oxygen-sensing conjugates discussed in this Section are summarized in Table 5.

6.2.2. *Delivery Methods Based on Nanomaterials*

Encapsulation within nanometer-sized particles provides a physical barrier between the luminescent sensing component and the environment while increasing the loading capacity over single stand-alone sensors. Nanomaterial sensors can be synthesized with a range of porosities designed to allow oxygen to readily diffuse and equilibrate with the surrounding environment. Moreover, they can be made to display a large surface density of functional groups, which can be used for conjugating targeting moieties. A summary of oxygen-sensitive nanomaterials is given in Table 6. The development of specific types of nanosensors for imaging applications, such as silica nanoparticles and hydrogel nanosensors, has been the subject of comprehensive recent reviews.[193,194]

Cell-uptake studies with oxygen-sensor-loaded nanoparticles formed by different polymeric materials indicated that although the nanoparticle interior can provide sufficient shielding from excessive oxygen quenching, the lack of a surface cell-targeting layer can result in inefficient cell internalization or increased toxicity.[195,196] To enhance cellular uptake, Koo Lee et al. recenly co-embedded Oxyphor G2 and an oxygen-insensitive dye (Alexa 647 dextran or HiLyte 680 SE) into polyacrylamide hydrogel nanoparticles bearing different targeting peptides.[197] The resulting nanoparticles were non-toxic, membrane-permeable, and tumor-specific ratiometric nanosensors.

The Papkovsky group also developed different types of cell-penetrating nanoparticle sensors,[198–200] using platinum(II) meso-tetrakis(pentafluorophenyl)porphyrin (PtTFPP) as the oxygen sensor embedded in methyl methacrylate and methacrylic acid based copolymers (poly(methyl methacrylate-*co*-methacrylic acid) (PMMA-MA) and Eudragit RL-100). The developed probes (Table 6) were applied in the dynamic monitoring of intracellular oxygen levels. The same porphyrin, PtTFPP, was recently used by the group of Wolfbeis to formulate three different phosphorescent nanoparticles possessing the same polystyrene (PS)/dodecyltrimethoxysilane (DTS) hybrid core but different surface layers, to produce a family of nanosensors that can assess mitochondrial dysfunction by reporting extracellular, intracellular, and intramitochondrial oxygenation.[201] Using different combinations of oxygen-sensing probes and polymer matrices, the Wolfbeis group has reported novel approaches for preparing sensor-doped nanoparticles.[202,203]

Polystyrene nanoparticles (PS-NPs) decorated with monoclonal antibodies (mAba) and doped with the NIR-emissive PdTBP sensor and a reference dye were synthesized by Napp and co-workers.[204] These were employed in both ratiometric dual-wavelength and lifetime-based oxygen sensing in in vitro studies with human mammary carcinoma cells as well as in vivo with tumor-bearing mice. Aside from improved targeting capabilities, novel nanoparticle designs have exploited the concepts of FRET and light upconversion for the mediated light activation of an encapsulated oxygen-sensing component. For example, Wu et al. reported a novel nanoparticle architecture consisting of π-conjugated polymer molecules doped with the oxygen sensor platinum(II) octaethylporpyrin (PtOEP),[205] where the polymer transfers its excitation energy to the porphyrin dye, resulting in oxygen-dependent phosphorescence emission. Sensor activation by light upconversion was achieved by Liu et al.[206] in the recent development of $[Ru(dpp)_3]^{2+}$ loaded, oxygen-sensitive nano-

Table 5: Conjugate oxygen probes and their applications.

Probe	Experimental system	Comments	Ref.
PtCP-BSA	FL5.12 human lymphoblastic cell line	facilitated transport required	[184,186]
PtCP-PEG	*E. coli* bacterial cells	facilitated transport required	[185]
PtCPK-BSA, PdCPK-BSA	A549, Jurkat, HeLa mammalian cells[a]	facilitated transport required	[186]
PtCP oligopeptides PtCP–bactenicin 7	mammalian and murine cells[a]	enhanced cellular uptake	[187] [188]
PtCP-arginine-rich peptides IrOEP oligopeptides	mammalian and murine cells[a] and MEF cells[b]	different sub-cellular localizations	[189] [190]
PtPFPP monosaccharides or short amino acids	PC12 multicellular spheroids, rat brain tissue slices	3D oxygenation imaging	[191]
Ru-Ahx-R8	myeloma cells, human blood platelets	accumulation in sub-cellular organelles	[192]

[a] A549: human lung adenocarcinoma epithelial cells; Jurkat: human T cell lymphoblast-like cells; HeLa: human cervical epithelial carcinoma; PC12: rat pheochromocytoma; HCT116: human colon carcinoma; HepG2: human hepatocellular liver carcinoma; SH-SY5Y: human neuroblastoma.
[b] MEF = murine embryonic fibroblasts.

Table 6: Nanoparticle formulations and their applications.

Probe/matrix	Experimental system	Comments	Ref.
$[Ru(dpp(SO_3Na)_2)_3]Cl_2$/ polyacrylamide	yeast cells, human adenosarcoma MCF-7	improved uptake by electroporation	[195]
Oxyphor R2/polysaccharide	embryo chorioallantoic membranes of chicks	toxicity decreases embryo viability	[196]
Oxyphor R2, Alexa647, or HiLyte 680 SE/ polyacrylamide hydrogel	A549, C6 glioma, and MCF-7 cells	ratiometric, coated with targeting peptides	[197]
PtTFPP/Eudragit RL-100 (NanO2)	mammalian and murine cells[a,b]	cationic, non-specific endocytosis	[198]
PtTFPP/PFO, Eudragit RL-100 (MM2)	MEF cells, embryonic rat neurosphere cultures	two-photon-excited, FRET-activated, multiple detection modalities	[199]
PtTFPP/PFO, PMMA-MA (PA2)	MEF, PC12 cells, 3D rat brain slices	anionic, ratiometric, two-photon excited	[200]
PtOEP/PFO, PDHF	J774 A1 murine cells	FRET-activated, brightly emissive	[205]
$[Ru(dpp)_3]^{2+}$/lanthanide-doped UCNPs	U87 MG human glioblastoma cells, zebrafish embryos	NIR-absorbing, activated by light upconversion	[206]
BF_2dbm(I)/PLA	breast-cancer 4T1 mammary carcinoma	ratiometric, tunable fluorescence/ phosphorescence emission	[207]
PdTPTBP/polystyrene	human carcinoma cells[c]	NIR-emitting, coated with PEG, antibodies for selective targeting	[204]

[a] PC12: rat pheochromocytoma; HCT116: human colon carcinoma; HepG2: human hepatocellular liver carcinoma; HeLa: human epithelial carcinoma; SH-SY5Y: human neuroblastoma. [b] MEF = murine embryonic fibroblasts. [c] SK-BR-3: human mammary carcinoma; AsPC1: human pancreatic adenocarcinoma cells

particles (dpp = 4,7-diphenyl-1,10-phenanthroline). An upconverting nanoparticle "antenna" absorbed NIR light and emitted blue photons that could excite $[Ru(dpp)_3]^{2+}$ (Figure 9). This NIR-absorbing nanosensor was applied in the imaging of oxygenation within living cells at different oxygen levels, as well as in the detection of induced cerebral anoxia in living zebrafish embryos.

Recently, an exciting design concept was introduced by Zhang et al. that involved the tuning of the fluorescence and room-temperature phosphorescence intensities in an iodide-substituted boron difluoride dibenzoylmethane (BF_2dbm(I)) analogue.[207] Coupling poly(lactic acid) (PLA) polymers of different chain lengths to the boron complex resulted in polymers whose fluorescence/phosphorescence ratio was modulated by changes in the molecular weight. The nanoparticles that were made from the polymer exhibited balanced fluorescence and phosphorescence intensities, and served as ratiometric imaging agents that enabled the in vivo quantification of

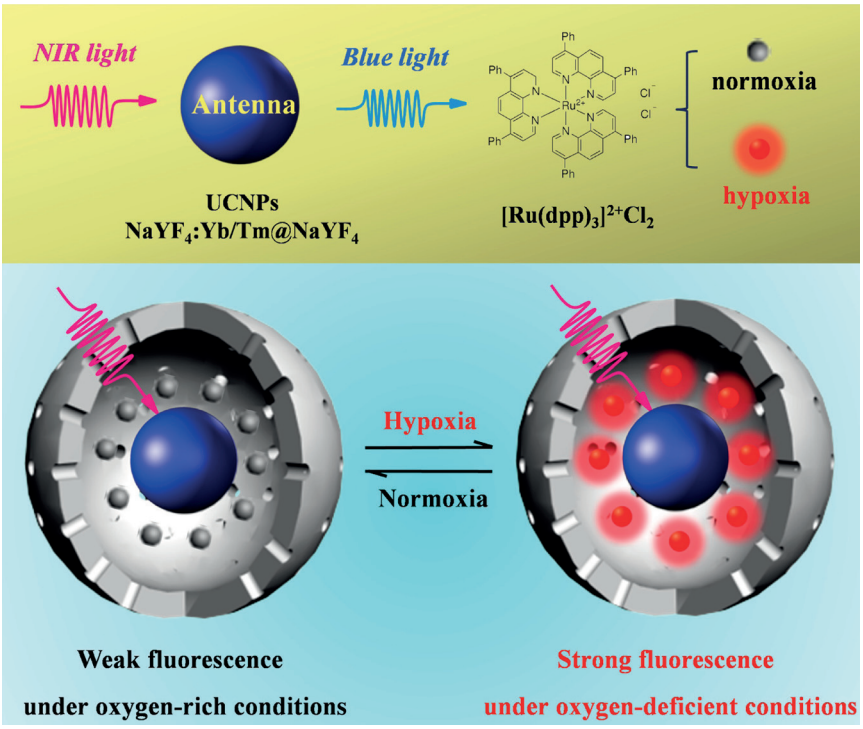

Figure 9. Light activation of the nanosensors, their structure, and their reversible, oxygen-dependent changes in luminescence emission. UCNPs = upconverted nanoparticles. Reproduced with permission from Ref. [206].

hypoxia in the tumor region of a mammary breast carcinoma in a mouse model.

6.2.3. *Fiber Optics, Sensor Films, and Sensor Foils*

Fiber-optic oxygen sensors incorporate luminescent materials on the fiber tip and operate using luminescence quenching. These fiber-optic oxygen-sensing tools can share the thin form of Clark electrodes, but are small and flexible, allowing for them to be used across a variety of environments. One example is OxyLite, a commercially available fiber-optic oxygen-sensing device that compares well to modern electrodes, such as those offered by Eppendorf. An article by Griffiths and Robinson presents a detailed comparison of the OxyLite and Eppendorf probes for tissue oxygenation measurements.[208] Similarly, Ocean Optics and PreSens offer fiber-optic probes for a variety of oxygen-sensing applications. Considerably greater detail on fiber-optic oxygen sensors and their applications in biological systems can be found in two recent comprehensive reviews that contain sections discussing this exciting class of oxygen probes.[209,210]

Other types of sensor formulations include films and foils impregnated with oxygen-sensing materials, which have been applied to the non-invasive in vivo imaging of tissue oxygenation for assessing viability during injury and diseases, as well as to monitor the progress of therapeutic interventions. The development of optical oxygen-sensing foils for tissue imaging was pioneered by Wolfbeis and co-workers,[211] and was first applied in monitoring oxygen gradients in engineered tissue. For the first in vivo applications, transparent planar sensors made by incorporating PtOEP into a polystyrene matrix were used for the measurement of surface pO_2 values over tumorous and normal tissue on the skin of hamsters using the dorsal skinfold chamber model.[212] Transcutaneous pO_2 imaging was additionally carried out in healthy human subjects to observe tourniquet-induced forearm ischemia. The transparent sensor foil was further refined by incorporating PdTBP as the oxygen sensor in poly(styrene-*co*-acrylonitrile) particles, which were then embedded in a biocompatible hydrogel matrix. This refined sensing foil was evaluated in monitoring wound surface pO_2 during healing at split-thickness skin graft donor sites that served as wound models.[213] In vivo 2D imaging using self-adhesive, ratiometric sensor foils was additionally applied for the monitoring of oxygenation of mice footpads to demonstrate the applicability of this technology to the detection of systemic hypoxia,[214] and to test the hypothesis that low tissue oxygen levels are characteristic in leishmanial skin lesions.[215] Recently, Lehner et al. reported a group of ultrasensitive optical oxygen sensors consisting of borondifluoride chelates and aluminum complexes that were embedded in polymer matrices and coated on glass slides to prepare very thin dried layers.[216] The new sensors showed significantly increased sensitivity for oxygen quantification, with detection limits as low as 7 pM in solution, but they have not yet been tested in biological systems.

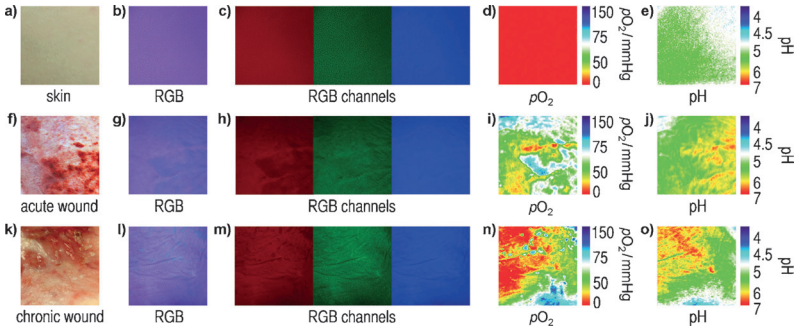

Figure 10. In vivo application of the dual pO_2 and pH sensor on the plain skin surface of the inner (volar) forearm (a–e), a skin graft donor site (postoperative, day 5) as a model for acute wound healing (f–j), and a chronic wound (k–o). Reproduced with permission from Ref. [217].

The concept of using optical sensing films was advanced by the Wolfbeis group with the development of a simultaneous dual-parameter imaging method for measuring both the pO_2 and pH values from a single image acquired with a conventional RGB digital camera.[217] Three chromophores were selected to match the RGB color space: the red oxygen sensor PtTPFPP, the green pH sensor fluorescein isothiocyanate (FITC), and the reference blue dye diphenylanthracene (DPA). These dyes were formulated into polymer microparticles and then incorporated in a biocompatible hydrogel. The potential of this method was demonstrated in the 2D imaging of the oxygen distribution and pH value in heterogeneous chronic wounds, where results indicated the detection of a sustained inflammatory phase (Figure 10). Using the same dual-parameter imaging concept, the oxygen sensor PdTBP, the pH sensor FITC, and the reference dye $[Ru(dpp)_3]^{2+}$ were independently embedded in microparticles and then incorporated in a biocompatible polyurethane hydrogel layer on transparent poly(vinylidene chloride) foils.[218]

The development of a transparent, colorimetric paint-on bandage was recently reported by Li et al.[143] The liquid bandage was formulated using the ester form of Oxyphor R2 and the reference dye Coumarin 500 embedded in a nitrocellulose matrix for applications in the 2D mapping of tissue oxygenation in skin, burns, and grafts. The sensing bandage was tested in vivo on a rat ischemic limb model as well as on porcine models of burn injuries (Figure 11) and skin grafts. This proof-of-concept study is the first step towards developing a quantitative, easy-to-use clinical diagnostic tool for mapping and quantifying the pO_2 values and oxygen consumption in wounds.

7. Conclusions and Outlook

The development of oxygen-sensing approaches has yielded a range of probes and methods that enable studies of the oxygen concentration from the whole-organ and -body scale to subcellular levels. From MRI to PET and from sensing foils to nanomaterials, the synthesis and design of oxygen sensors have met both research and clinical needs. Large-scale imaging toolkits can now generate oxygenation

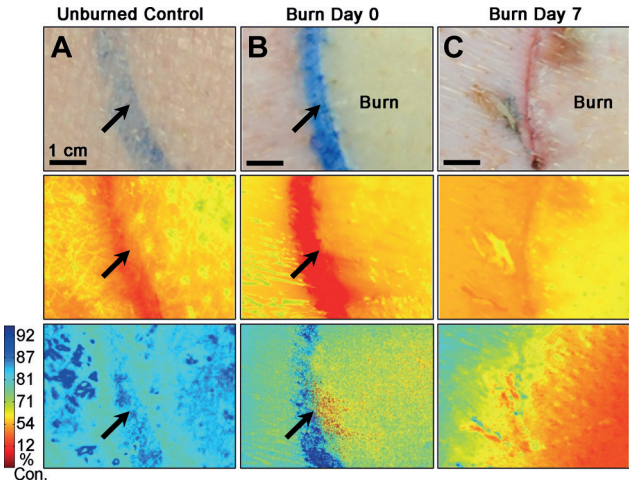

Figure 11. Progression of a full-thickness burn on a porcine model of burn injury monitored by an oxygen-sensing paint-on bandage. A) Unburned control, B) immediately post-burn, and C) seven days post-burn. Top row: regular photographs; middle row: emission at $\lambda = 700$ nm showing the skin autofluorescence; bottom row: oxygen-consumption maps (%) obtained after eliminating autofluorescence. Blue and red indicate higher and lower oxygen consumption by the tissues, respectively. Arrows indicate ink marks dividing burn and surrounding skin. Reproduced with permission from Ref. [143].

maps in humans and provide detailed insight into both disease mechanisms and treatment response. At the microscale, oxygen sensors have enabled researchers to visualize and quantify cellular and subcellular oxygen gradients during physiological and disease perturbations. Future developments in oxygen-sensing technology will take place on two fronts: further developments of materials and methods while focusing on research needs, and the translation of current technologies from the bench to the bedside.

To build the next generation of oxygen-sensing toolkits for biomedical research, the wider research community should be engaged in creating probes and methods that can be used outside of the specific fields of porphyrin, dendrimer, or nanoparticle chemistry. Whereas past research has been highly successful in exploring the myriad of parameters in instrumentation and probe design, the accumulated knowledge in these fields must now be focused on specific applications. In the fields of cancer research, brain science, cardiology, and pulmonology, for example, there is a need to understand not only vascular oxygenation, but also the oxygenation within solid tissues. Ischemic injuries, hypoxic tumor regions, and stroke, for example, are all conditions where a precise spatiotemporal knowledge of tissue oxygenation is required. Even though MR and PET research has significantly advanced our understanding of oxygen consumption and supply, the vast majority of MR and PET oxygen-sensing tools are focused on the vasculature. Further information is needed to better understand the consequences of such conditions and to improve current treatments. Our knowledge in this area would be considerably advanced by the development of oxygen sensors that are taken up into tissues, either passively or through targeting approaches. Chemical toolkits that enable sensor delivery through the bloodstream to select sites would be highly advantageous and are already in development. This is a considerable challenge, especially in the case of ischemic tissues and cancer, where hypoxic regions can lie many cell layers away from the blood supply. In the case of ischemic injuries, it can be difficult to deliver exogenous agents through damaged vessels. Likewise, in cancer, hypoxic cell populations can exist in areas poorly fed by the abnormal and leaky tumor-associated vasculature. Strategies are needed that can actively drive oxygen-sensing probes out of vessels into inflamed, damaged, and dense tissue.

Another barrier that must be overcome for routine oxygen sensing for demanding biological research applications is the sensitivity of the oxygen sensors themselves. In the optical sensing space, numerous luminescent sensors have been developed, but many of these suffer from poor quantum efficiencies, making their emission dim and difficult to detect. This has forced researchers to use special high-sensitivity detectors, which can be expensive, to make use of high sensor concentrations, which can perturb cells and tissues, or simply to deal with low signal-to-noise ratios. Oxygen sensors with far greater quantum efficiencies are needed for mainstream oxygen quantification research. This will act to simplify the instrumentation required to visualize the signals that are emitted by these sensors, making less expensive, less specialized toolkits widely available to more research efforts.

Such efforts may also unlock combined approaches that enable researchers to utilize both macro- and microscale imaging toolkits for oxygen studies. Future research efforts would benefit from multiplexed oxygen sensors that are, for example, capable of both PET and optical detection for a first macroscopic exploration followed by microscopic intravital imaging. Not only valuable for research, such combined platforms would be highly useful in the clinical space, enabling physicians to glean both tissue- and cellular-level oxygenation information. For example, multimodality imaging and sensing is becoming increasingly important in both cancer research and clinical care, and could be a potential first target for the combination of different oxygen tension detection tools. The translation of such tools will likely be difficult, as regulatory hurdles are currently preventing oxygen-imaging sensors from reaching patients. For example, the siloxane probes that enable proton MRI sensing of vascular oxygenation, while potent, are still not FDA-approved. The only molecular optical oxygen sensor currently FDA-approved is PpIX, which has a relatively low signal-to-noise ratio and can cause unwanted photosensitization of tissues.

The barriers to clinical care will be far lower for surface oxygen-sensing applications. The development of planar arrays of oxygen electrodes for two-dimensional skin oxygen mapping, for example, will likely face a more straightforward regulatory approval. Sensing foils and bandages for optical oxygen sensing may also have lower barriers to adoption, as they provide easy-to-read oxygenation maps of the skin surface. The development of brighter optical oxygen sensors would significantly aid these efforts, and may enable the design of bandages that can easily be read out with the naked eye under ambient light conditions. When combined with portable, compact readout devices, such as cellular

phones, and wearables, such as Google Glass, these oxygen-sensing tools could be brought not only into field use, but also directly to the patient for applications, such as home care.

We would like to thank Dr. Lauren A. Austin, Nicholas Nowell, Michael J. Murphy, and the rest of the Evans team for their help with editing this manuscript.

How to cite: *Angew. Chem. Int. Ed.* **2015**, *54*, 8340 – 8362
Angew. Chem. **2015**, *127*, 8458 – 8483

[1] B. M. Koeppen, B. A. Stanton, *Berne & Levy Physiology*, 6th. ed., Mosby Elsevier, Philadelphia, **2008**.
[2] A. Carreau, B. El Hafny-Rahbi, A. Matejuk, C. Grillon, C. Kieda, *J. Cell. Mol. Med.* **2011**, *15*, 1239 – 1253.
[3] V. Dhawan, M. DeGeorgia, *J. Neurointerv. Surg.* **2012**, *4*, 407 – 413.
[4] A. J. Brooks, J. S. Hammond, K. Girling, I. J. Beckingham, *J. Surg. Res.* **2007**, *141*, 247 – 251.
[5] G. H. Danet, *J. Clin. Invest.* **2003**, *112*, 126 – 135.
[6] K. Parmar, P. Mauch, J.-A. Vergilio, R. Sackstein, J. D. Down, *Proc. Natl. Acad. Sci. USA* **2007**, *104*, 5431 – 5436.
[7] J. A. Spencer, F. Ferraro, E. Roussakis, A. Klein, J. Wu, J. M. Runnels, W. Zaher, L. J. Mortensen, C. Alt, R. Turcotte, R. Yusuf, D. Cote, S. A. Vinogradov, D. T. Scadden, C. P. Lin, *Nature* **2014**, *508*, 269 – 273.
[8] J. Yu, W. Cui, D. Zhao, R. P. Mason in *Fluorine and Health* (Ed.: A. Tressaud), Elsevier, Amsterdam, **2008**, pp. 197 – 276.
[9] L. S. Lilly, H. M. School, *Pathophysiology of Heart Disease: A Collaborative Project of Medical Students and Faculty*, Wolters Kluwer/Lippincott Williams & Wilkins, **2011**.
[10] M. Carrier, S. Trudelle, P. Thai, L. Pelletier, *J. Cardiovasc. Surg.* **1998**, *39*, 593 – 597.
[11] B. R. Soller, C. Hsi, J. Favreau, N. Cingo, R. A. Lancey, O. N. Okike, T. J. Vander Salm, *J. Cardiovasc. Surg.* **2004**, *19*, 167 – 174.
[12] S. r. E. Pischke, C. Tronstad, L. Holhjem, P. S. Halvorsen, T. I. Tønnessen, *Eur. J. Cardiothorac. Surg.* **2012**, *42*, 157 – 163.
[13] W. R. Wilson, M. P. Hay, *Nat. Rev. Cancer* **2011**, *11*, 393 – 410.
[14] D. Hanahan, R. Weinberg, *Cell* **2000**, *100*, 57 – 70.
[15] J. Folkman, *Annu. Rev. Med.* **2006**, *57*, 1 – 18.
[16] J. Folkman, *Nat. Rev. Drug Discovery* **2007**, *6*, 273 – 286.
[17] D. Hanahan, R. A. Weinberg, *Cell* **2011**, *144*, 646 – 674.
[18] D. Ackerman, M. C. Simon, *Trends Cell Biol.* **2014**, *24*, 472 – 478.
[19] R.-h. Xu, H. Pelicano, Y. Zhou, J. S. Carew, L. Feng, K. N. Bhalla, M. J. Keating, P. Huang, *Cancer Res.* **2005**, *65*, 613 – 621.
[20] X. Song, X. Liu, W. Chi, Y. Liu, L. Wei, X. Wang, J. Yu, *Cancer Chemother. Pharmacol.* **2006**, *58*, 776 – 784.
[21] J. M. Brown, *Methods Enzymol.* **2007**, *435*, 297 – 321.
[22] N. Rohwer, T. Cramer, *Drug Resist. Updates* **2011**, *14*, 191 – 201.
[23] S. Koch, F. Mayer, F. Honecker, M. Schittenhelm, C. Bokemeyer, *Br. J. Cancer* **2003**, *89*, 2133 – 2139.
[24] J. G. Rajendran, K. A. Krohn, *Radiol. Clin. North Am.* **2005**, *43*, 169 – 187.
[25] J. P. Celli, I. Rizvi, C. L. Evans, A. O. Abu-Yousif, T. Hasan, *J. Biomed. Opt.* **2010**, *15*, 051603.
[26] C. L. Evans, A. O. Abu-Yousif, Y. J. Park, O. J. Klein, J. P. Celli, I. Rizvi, X. Zheng, T. Hasan, *PLoS One* **2011**, *6*, e23434.
[27] O. J. Klein, B. Bhayana, Y. J. Park, C. L. Evans, *Mol. Pharmaceutics* **2012**, *9*, 3171 – 3182.
[28] L. C. Clark, R. Wolf, D. Granger, Z. Taylor, *J. Appl. Physiol.* **1953**, *6*, 189 – 193.
[29] D. G. Buerk, *Methods Enzymol.* **2004**, *381*, 665 – 690.
[30] M. Nozue, I. Lee, F. Yuan, B. A. Teicher, D. M. Brizel, M. W. Dewhirst, C. G. Milross, L. Milas, C. W. Song, C. D. Thomas, M. Guichard, S. M. Evans, C. J. Koch, E. M. Lord, R. K. Jain, H. D. Suit, *J. Surg. Oncol.* **1997**, *66*, 30 – 38.
[31] G. Mees, R. Dierckx, C. Vangestel, C. Van de Wiele, *Eur. J. Nucl. Med. Mol. Imaging* **2009**, *36*, 1674 – 1686.
[32] A. Baskin, F. Buchegger, Y. Seimbille, O. Ratib, V. Garibotto, *Curr. Vasc. Pharmacol.* **2015**, *13*, 209 – 217.
[33] J. L. Tatum, G. J. Kelloff, R. J. Gillies, J. M. Arbeit, J. M. Brown, K. S. Chao, J. D. Chapman, W. C. Eckelman, A. W. Fyles, A. J. Giaccia, R. P. Hill, C. J. Koch, M. C. Krishna, K. A. Krohn, J. S. Lewis, R. P. Mason, G. Melillo, A. R. Padhani, G. Powis, J. G. Rajendran, R. Reba, S. P. Robinson, G. L. Semenza, H. M. Swartz, P. Vaupel, D. Yang, B. Croft, J. Hoffman, G. Liu, H. Stone, D. Sullivan, *Int. J. Radiat. Biol.* **2006**, *82*, 699 – 757.
[34] K. A. Krohn, J. M. Link, R. P. Mason, *J. Nucl. Med.* **2008**, *49*, 129S – 148S.
[35] T. Christen, D. S. Bolar, G. Zaharchuk, *Am. J. Neuroradiol.* **2013**, *34*, 1113 – 1123.
[36] H. M. Swartz, N. Khan, J. Buckey, R. Comi, L. Gould, O. Grinberg, A. Hartford, H. Hopf, H. Hou, E. Hug, A. Iwasaki, P. Lesniewski, I. Salikhov, T. Walczak, *NMR Biomed.* **2004**, *17*, 335 – 351.
[37] R. J. Gillies, N. Raghunand, G. S. Karczmar, Z. M. Bhujwalla, *J. Magn. Reson. Imaging* **2002**, *16*, 430 – 450.
[38] B. Gallez, C. Baudelet, B. F. Jordan, *NMR Biomed.* **2004**, *17*, 240 – 262.
[39] J. E. Sinex, *Am. J. Emerg. Med.* **1999**, *17*, 59 – 66.
[40] D. Boas, D. Brooks, E. Miller, C. DiMarzio, M. Kilmer, R. Gaudette, Q. Zhang, *IEEE Signal Process. Mag.* **2001**, *18*, 57 – 75.
[41] B. J. Tromberg, B. W. Pogue, K. D. Paulsen, A. G. Yodh, D. A. Boas, A. E. Cerussi, *Med. Phys.* **2008**, *35*, 2443 – 2451.
[42] L. V. Wang, *Med. Phys.* **2008**, *35*, 5758 – 5767.
[43] L. V. Wang, S. Hu, *Science* **2012**, *335*, 1458 – 1462.
[44] R. V. Kuranov, S. Kazmi, A. B. McElroy, J. W. Kiel, A. K. Dunn, T. E. Milner, T. Q. Duong, *Opt. Express* **2011**, *19*, 23831 – 23844.
[45] D. J. Faber, E. G. Mik, M. C. Aalders, T. G. van Leeuwen, *Opt. Lett.* **2005**, *30*, 1015 – 1017.
[46] R. I. Dmitriev, D. B. Papkovsky, *Cell. Mol. Life Sci.* **2012**, *69*, 2025 – 2039.
[47] M. Quaranta, S. Borisov, I. Klimant, *Bioanal. Rev.* **2012**, *4*, 115 – 157.
[48] S. A. Vinogradov, D. F. Wilson in *Designing Dendrimers*, *1st ed.* (Eds.: S. Campagna, P. Ceroni, F. Puntoriero), Wiley, Hoboken, **2012**, Chap. 12, pp. 463 – 503.
[49] D. B. Papkovsky, R. I. Dmitriev, *Chem. Soc. Rev.* **2013**, *42*, 8700 – 8732.
[50] X.-d. Wang, O. S. Wolfbeis, *Chem. Soc. Rev.* **2014**, *43*, 3666 – 3761.
[51] M. W. Dewhirst, B. Klitzman, R. D. Braun, D. M. Brizel, Z. A. Haroon, T. W. Secomb, *Int. J. Cancer* **2000**, *90*, 237 – 255.
[52] W. L. Yip, *Int. Wound J.* **2014**, DOI: 10.1111/iwj.12356.
[53] K. I. Jang, S. Y. Han, S. Xu, K. E. Mathewson, Y. Zhang, J. W. Jeong, G. T. Kim, R. C. Webb, J. W. Lee, T. J. Dawidczyk, R. H. Kim, Y. M. Song, W. H. Yeo, S. Kim, H. Cheng, S. I. Rhee, J. Chung, B. Kim, H. U. Chung, D. Lee, Y. Yang, M. Cho, J. G. Gaspar, R. Carbonari, M. Fabiani, G. Gratton, Y. Huang, J. A. Rogers, *Nat. Commun.* **2014**, *5*, 4779.
[54] D. S. Vikram, J. L. Zweier, P. Kuppusamy, *Antioxid. Redox Signaling* **2007**, *9*, 1745 – 1756.
[55] J. C. Baron, M. G. Bousser, D. Comar, F. Soussaline, P. Castaigne, *Eur. Neurol.* **1981**, *20*, 273 – 284.
[56] J. C. Baron, M. G. Bousser, A. Rey, A. Guillard, D. Comar, P. Castaigne, *Stroke* **1981**, *12*, 454 – 459.
[57] Y. Magata, T. Temma, H. Iida, M. Ogawa, T. Mukai, Y. Iida, T. Morimoto, J. Konishi, H. Saji, *J. Cereb. Blood Flow Metab.* **2003**, *23*, 671 – 676.

[58] G. Sette, J. C. Baron, B. Mazoyer, M. Levasseur, S. Pappata, C. Crouzel, *Brain* **1989**, *112*, 931 – 951.
[59] A. Hino, Y. Imahori, H. Tenjin, N. Mizukawa, S. Ueda, K. Hirakawa, H. Nakahashi, *Neurosurgery* **1990**, *26*, 615 – 621.
[60] H. Tenjin, S. Ueda, N. Mizukawa, Y. Imahori, A. Hino, T. Yamaki, T. Kuboyama, T. Ebisu, K. Hirakawa, M. Yamashita, H. Nakahashi, *Neurosurgery* **1990**, *26*, 971 – 979.
[61] P. Vespa, M. Bergsneider, N. Hattori, H.-M. Wu, S.-C. Huang, N. A. Martin, T. C. Glenn, D. L. McArthur, D. A. Hovda, *J. Cereb. Blood Flow Metab.* **2005**, *25*, 763 – 774.
[62] J. P. Coles, T. D. Fryer, M. R. Coleman, P. Smielewski, A. K. Gupta, P. S. Minhas, F. Aigbirhio, D. A. Chatfield, G. B. Williams, S. Boniface, T. A. Carpenter, J. C. Clark, J. D. Pickard, D. K. Menon, *Crit. Care Med.* **2007**, *35*, 568 – 578.
[63] D. K. Menon, J. P. Coles, A. K. Gupta, T. D. Fryer, P. Smielewski, D. A. Chatfield, F. Aigbirhio, J. N. Skepper, P. S. Minhas, P. J. Hutchinson, T. A. Carpenter, J. C. Clark, J. D. Pickard, *Crit. Care Med.* **2004**, *32*, 1384 – 1390.
[64] M. G. Abate, M. Trivedi, T. D. Fryer, P. Smielewski, D. A. Chatfield, G. B. Williams, F. Aigbirhio, T. A. Carpenter, J. D. Pickard, D. K. Menon, J. P. Coles, *Neurocrit. Care* **2008**, *9*, 319 – 325.
[65] M. Lubberink, Y. Y. Wong, P. G. Raijmakers, R. C. Schuit, G. Luurtsema, R. Boellaard, P. Knaapen, A. Vonk-Noordegraaf, A. A. Lammertsma, *J. Nucl. Med.* **2011**, *52*, 60 – 66.
[66] G. Marchal, C. Serrati, P. Rioux, M. C. Petit-Taboue, F. Viader, V. Delasayette, F. Ledoze, P. Lochon, J. M. Derlon, J. M. Orgogozo, J. C. Baron, *Lancet* **1993**, *341*, 925 – 927.
[67] Y. Maeda, Y. Kawasaki, I. Jibiki, N. Yamaguchi, H. Matsuda, K. Hisada, *Eur. Neurol.* **1991**, *31*, 380 – 383.
[68] H. S. Markus, A. J. Lees, G. Lennox, C. D. Marsden, D. C. Costa, *Mov. Disord.* **1995**, *10*, 179 – 187.
[69] T. Suzuki, K. Ogasawara, H. Kuroda, K. Chida, K. Aso, M. Kobayashi, S. Fujiwara, K. Yoshida, K. Terasaki, A. Ogawa, *Nucl. Med. Commun.* **2012**, *33*, 171 – 178.
[70] R. J. Derick in *Hevener's Ocular Pharmacology*, *6th. ed.*, CV Mosby Co, St. Louis, **1994**, pp. 78 – 99.
[71] K. Ogasawara, N. Tomitsuka, M. Kobayashi, N. Komoribayashi, T. Kukuda, H. Saitoh, T. Inoue, A. Ogawa, *Neurol. Med. Chir. (Tokyo)* **2006**, *46*, 161 – 163.
[72] H. Saito, K. Ogasawara, T. Suzuki, H. Kuroda, M. Kobayashi, K. Yoshida, Y. Kubo, A. Ogawa, *Neurol. Med. Chir. (Tokyo)* **2011**, *51*, 479 – 483.
[73] H. Yamauchi, H. Fukuyama, K. Harada, H. Nabatame, M. Ogawa, Y. Ouchi, J. Kimura, J. Konishi, *Arch. Neurol.* **1993**, *50*, 1070 – 1074.
[74] N. Oku, T. Kashiwagi, J. Hatazawa, *Ann. Nucl. Med.* **2010**, *24*, 629 – 638.
[75] V. D. Kodibagkar, X. Wang, R. P. Mason, *Front. Biosci.* **2008**, *13*, 1371 – 1384.
[76] J. X. Yu, R. R. Hallac, S. Chiguru, R. P. Mason, *Prog. Nucl. Magn. Reson. Spectrosc.* **2013**, *70*, 25 – 49.
[77] J.-J. Delpuecha, M. A. Hamza, G. Serratrice, M.-J. Stébé, *J. Chem. Phys.* **1979**, *70*, 2680 – 2687.
[78] R. P. Mason, R. L. Nunnally, P. P. Antich, *Magn. Reson. Med.* **1991**, *18*, 71 – 79.
[79] D. Zhao, S. Ran, A. Constantinescu, E. W. Hahn, R. P. Mason, *Neoplasia* **2003**, *5*, 308 – 318.
[80] S. A. Wickline, R. P. Mason, S. D. Caruthers, J. Chen, P. M. Winter, M. S. Hughes, G. M. Lanza in *Fluorocarbon Agents for Quantitative Multimodal Molecular Imaging and Targeted Therapeutics* (Eds.: R. Weissleder, S. S. Gambhir, B. D. Ross, A. Rehemtulla), BC Decker Inc., Hamilton, **2010**, pp. 542 – 573.
[81] S. R. Thomas, R. G. Pratt, R. W. Millard, R. C. Samaratunga, Y. Shiferaw, L. C. Clark, R. E. Hoffmann, *J. Magn. Reson. Imaging* **1994**, *4*, 631 – 635.
[82] C.-S. Lai, S. J. Stair, H. Miziorko, J. S. Hyde, *J. Magn. Reson.* **1969**, *57*, 447 – 452.
[83] B. P. van der Sanden, A. Heerschap, A. W. Simonetti, P. F. Rijken, H. P. Peters, G. Stüben, A. J. van der Kogel, *Int. J. Radiat. Oncol. Biol. Phys.* **1999**, *44*, 649 – 658.
[84] R. P. Mason, P. P. Antich, E. E. Babcock, A. Constantinescu, P. Peschke, E. W. Hahn, *Int. J. Radiat. Oncol. Biol. Phys.* **1994**, *29*, 95 – 103.
[85] H. T. Tran, Q. Guo, D. J. Schumacher, R. B. Buxton, R. F. Mattrey, *Acad. Radiol.* **1995**, *2*, 756 – 761.
[86] D. Eidelberg, G. Johnson, D. Barnes, P. S. Tofts, D. Delpy, D. Plummer, W. I. McDonald, *Magn. Reson. Med.* **1988**, *6*, 344 – 352.
[87] S. R. Thomas, R. G. Pratt, R. W. Millard, R. C. Samaratunga, Y. Shiferaw, A. J. McGoron, K. K. Tan, *Magn. Reson. Imaging* **1996**, *14*, 103 – 114.
[88] B. F. Jordan, G. O. Cron, B. Gallez, *Magn. Reson. Med.* **2009**, *61*, 634 – 638.
[89] S. Liu, S. J. Shah, L. J. Wilmes, J. Feiner, V. D. Kodibagkar, M. F. Wendland, R. P. Mason, N. Hylton, H. W. Hopf, M. D. Rollins, *Magn. Reson. Med.* **2011**, *66*, 1722 – 1730.
[90] D. Zhao, L. Jiang, E. W. Hahn, R. P. Mason, *Int. J. Radiat. Oncol. Biol. Phys.* **2005**, *62*, 872 – 880.
[91] C. Diepart, O. Karroum, J. Magat, O. Feron, J. Verrax, P. B. Calderon, V. Grégoire, P. Leveque, J. Stockis, N. Dauguet, B. F. Jordan, B. Gallez, *Cancer Res.* **2012**, *72*, 482 – 490.
[92] D. K. Kadayakkara, J. M. Janjic, L. K. Pusateri, W. B. Young, E. T. Ahrens, *Magn. Reson. Med.* **2010**, *64*, 1252 – 1259.
[93] S. Ogawa, T. M. Lee, A. R. Kay, D. W. Tank, *Proc. Natl. Acad. Sci. USA* **1990**, *87*, 9868 – 9872.
[94] S. Ogawa, T. M. Lee, A. S. Nayak, P. Glynn, *Magn. Reson. Med.* **1990**, *14*, 68 – 78.
[95] A. R. Padhani, K. A. Krohn, J. S. Lewis, M. Alber, *Eur. Radiol.* **2007**, *17*, 861 – 872.
[96] F. A. Howe, S. P. Robinson, D. J. McIntyre, M. Stubbs, J. R. Griffiths, *NMR Biomed.* **2001**, *14*, 497 – 506.
[97] H. An, W. Lin, *J. Cereb. Blood Flow Metab.* **2000**, *20*, 1225 – 1236.
[98] D. A. Yablonskiy, A. L. Sukstanskii, X. He, *NMR Biomed.* **2013**, *26*, 963 – 986.
[99] N. P. Blockley, V. E. Griffeth, A. B. Simon, R. B. Buxton, *NMR Biomed.* **2013**, *26*, 987 – 1003.
[100] C. Baudelet, B. Gallez, *Curr. Med. Imaging Rev.* **2005**, *1*, 229 – 243.
[101] J. F. Dunn, J. A. O'Hara, Y. Zaim-Wadghiri, H. Lei, M. E. Meyerand, O. Y. Grinberg, H. Hou, P. J. Hoopes, E. Demidenko, H. M. Swartz, *J. Magn. Reson. Imaging* **2002**, *16*, 511 – 521.
[102] K. Matsumoto, M. Bernardo, S. Subramanian, P. Choyke, J. B. Mitchell, M. C. Krishna, M. J. Lizak, *Magn. Reson. Med.* **2006**, *56*, 240 – 246.
[103] Z. Zhang, R. R. Hallac, P. Peschke, R. P. Mason, *Magn. Reson. Med.* **2014**, *71*, 561 – 569.
[104] J. P. O'Connor, J. H. Naish, A. Jackson, J. C. Waterton, Y. Watson, S. Cheung, D. L. Buckley, D. M. McGrath, G. A. Buonaccorsi, S. J. Mills, C. Roberts, G. C. Jayson, G. J. Parker, *Magn. Reson. Med.* **2009**, *61*, 75 – 83.
[105] V. D. Kodibagkar, X. Wang, J. Pacheco-Torres, P. Gulaka, R. P. Mason, *NMR Biomed.* **2008**, *21*, 899 – 907.
[106] P. K. Gulaka, U. Rastogi, M. A. McKay, X. Wang, R. P. Mason, V. D. Kodibagkar, *NMR Biomed.* **2011**, *24*, 1226 – 1234.
[107] V. H. Liu, C. C. Vassiliou, S. M. Imaad, M. J. Cima, *Proc. Natl. Acad. Sci. USA* **2014**, *111*, 6588 – 6593.
[108] V. D. Kodibagkar, W. Cui, M. E. Merritt, R. P. Mason, *Magn. Reson. Med.* **2006**, *55*, 743 – 748.
[109] B. Gallez, K. Mader, *Free Radical Biol. Med.* **2000**, *29*, 1078 – 1084.

[110] H. Hou, O. Y. Grinberg, S. Taie, S. Leichtweis, M. Miyake, S. Grinberg, H. Xie, M. Csete, H. M. Swartz, *Anesth. Analg.* **2003**, *96*, 1467 – 1472.
[111] P. Kuppusamy, M. Chzhan, K. Vij, M. Shteynbuk, D. J. Lefer, E. Giannella, J. L. Zweier, *Proc. Natl. Acad. Sci. USA* **1994**, *91*, 3388 – 3392.
[112] G. He, R. A. Shankar, M. Chzhan, A. Samouilov, P. Kuppusamy, J. L. Zweier, *Proc. Natl. Acad. Sci. USA* **1999**, *96*, 4586 – 4591.
[113] K. J. Liu, P. Gast, M. Moussavi, S. W. Norby, N. Vahidi, T. Walczak, M. Wu, H. M. Swartz, *Proc. Natl. Acad. Sci. USA* **1993**, *90*, 5438 – 5442.
[114] T. Nakashima, F. Goda, J. Jiang, T. Shima, H. M. Swartz, *Magn. Reson. Med.* **1995**, *34*, 888 – 892.
[115] P. E. James, G. Bacic, O. Y. Grinberg, F. Goda, J. F. Dunn, S. K. Jackson, H. M. Swartz, *Free Radical Biol. Med.* **1996**, *21*, 25 – 34.
[116] M. Krzic, M. Sentjurc, J. Kristl, *J. Controlled Release* **2001**, *70*, 203 – 211.
[117] H. J. Halpern, C. Yu, M. Peric, E. Barth, D. J. Grdina, B. A. Teicher, *Proc. Natl. Acad. Sci. USA* **1994**, *91*, 13047 – 13051.
[118] M. Elas, J. M. Magwood, B. Butler, C. Li, R. Wardak, R. DeVries, E. D. Barth, B. Epel, S. Rubinstein, C. A. Pelizzari, R. R. Weichselbaum, H. J. Halpern, *Cancer Res.* **2013**, *73*, 5328 – 5335.
[119] N. Khan, B. B. Williams, H. Hou, H. Li, H. M. Swartz, *Antioxid. Redox Signaling* **2007**, *9*, 1169 – 1182.
[120] B. Chen, B. W. Pogue, I. A. Goodwin, J. A. O'Hara, C. M. Wilmot, J. E. Hutchins, P. J. Hoopes, T. Hasan, *Radiat. Res.* **2003**, *160*, 452 – 459.
[121] M. C. Krishna, S. English, K. Yamada, J. Yoo, R. Murugesan, N. Devasahayam, J. A. Cook, K. Golman, J. H. Ardenkjaer-Larsen, S. Subramanian, J. B. Mitchell, *Proc. Natl. Acad. Sci. USA* **2002**, *99*, 2216 – 2221.
[122] D. Grucker, J. Chambron, *Magn. Reson. Imaging* **1993**, *11*, 691 – 696.
[123] T. Durduran, R. Choe, W. Baker, A. Yodh, *Rep. Prog. Phys.* **2010**, *73*, 076701.
[124] A. Villringer, B. Chance, *Trends Neurosci.* **1997**, *20*, 435 – 442.
[125] J. Yi, Q. Wei, W. Liu, V. Backman, H. F. Zhang, *Opt. Lett.* **2013**, *38*, 1796 – 1798.
[126] Y. Mendelson, *Clin. Chem.* **1992**, *38*, 1601 – 1607.
[127] W. A. Bowes III, Jr., B. C. Corke, J. Hulka, *Obstet. Gynecol.* **1989**, *74*, 541 – 546.
[128] R. Choe in Engineering in Medicine and Biology Society, 2009. EMBC 2009. Annual International Conference of the IEEE, pp. 6335 – 6337.
[129] M. Simick, L. Lilge, *Br. J. Radiol.* **2014**, *78*, 1009 – 1017.
[130] B. W. Pogue, S. C. Davis, X. Song, B. A. Brooksby, H. Dehghani, K. D. Paulsen, *J. Biomed. Opt.* **2006**, *11*, 033001.
[131] C.-W. Lu, C.-K. Lee, M.-T. Tsai, Y.-M. Wang, C. Yang, *Opt. Lett.* **2008**, *33*, 416 – 418.
[132] R. V. Kuranov, J. Qiu, A. B. McElroy, A. Estrada, A. Salvaggio, J. Kiel, A. K. Dunn, T. Q. Duong, T. E. Milner, *Biomed. Opt. Express* **2011**, *2*, 491 – 504.
[133] W. L. Rumsey, J. M. Vanderkooi, D. F. Wilson, *Science* **1988**, *241*, 1649 – 1651.
[134] J. M. Vanderkooi, G. Maniara, T. J. Green, D. F. Wilson, *J. Biol. Chem.* **1987**, *262*, 5476 – 5482.
[135] X. D. Wang, R. J. Meier, M. Link, O. S. Wolfbeis, *Angew. Chem. Int. Ed.* **2010**, *49*, 4907 – 4909; *Angew. Chem.* **2010**, *122*, 5027 – 5029.
[136] A. J. Nichols, E. Roussakis, O. J. Klein, C. L. Evans, *Angew. Chem. Int. Ed.* **2014**, *53*, 3671 – 3674; *Angew. Chem.* **2014**, *126*, 3745 – 3748.
[137] R. J. Woods, S. Scypinski, L. J. C. Love, *Anal. Chem.* **1984**, *56*, 1395 – 1400.
[138] R. M. Ballew, J. N. Demas, *Anal. Chem.* **1989**, *61*, 30 – 33.
[139] B. Valeur, *Molecular Fluorescence*: *Principles and Applications*, Wiley-VCH, Weinheim, **2001**.
[140] M. I. J. Stich, L. H. Fischer, O. S. Wolfbeis, *Chem. Soc. Rev.* **2010**, *39*, 3102 – 3114.
[141] S. A. Vinogradov, M. A. Fernandez-Searra, B. W. Dugan, D. F. Wilson, *Rev. Sci. Instrum.* **2001**, *72*, 3396.
[142] D. F. Wilson, S. A. Vinogradov, B. W. Dugan, D. Biruski, L. Waldron, S. A. Evans, *Comp. Biochem. Physiol. Part A* **2002**, *132*, 153 – 159.
[143] Z. Li, E. Roussakis, P. G. L. Koolen, A. M. S. Ibrahim, K. Kim, L. F. Rose, J. Wu, A. J. Nichols, Y. Baek, R. Birngruber, G. Apiou-Sbirlea, R. Matyal, T. Huang, R. Chan, S. J. Lin, C. L. Evans, *Biomed. Opt. Express* **2014**, *5*, 3748 – 3764.
[144] M. Ranji, D. L. Jaggard, S. V. Apreleva, S. A. Vinogradov, B. Chance, *Opt. Lett.* **2006**, *31*, 2995 – 2997.
[145] L. S. Ziemer, W. M. F. Lee, S. A. Vinogradov, C. Sehgal, D. F. Wilson, *J. Appl. Physiol.* **2005**, *98*, 1503 – 1510.
[146] R. Shonat, A. Kight, *Ann. Biomed. Eng.* **2003**, *31*, 1084 – 1096.
[147] S. Sakadzic, E. Roussakis, M. A. Yaseen, E. T. Mandeville, V. J. Srinivasan, K. Arai, S. Ruvinskaya, A. Devor, E. H. Lo, S. A. Vinogradov, D. A. Boas, *Nat. Methods* **2010**, *7*, 755 – 759.
[148] I. Gryczynski, Z. Gryczynski, G. Rao, J. R. Lakowicz, *Analyst* **1999**, *124*, 1041 – 1044.
[149] T. Yoshihara, Y. Yamaguchi, M. Hosaka, T. Takeuchi, S. Tobita, *Angew. Chem. Int. Ed.* **2012**, *51*, 4148 – 4151; *Angew. Chem.* **2012**, *124*, 4224 – 4227.
[150] J. Lecoq, A. Parpaleix, E. Roussakis, M. Ducros, Y. G. Houssen, S. A. Vinogradov, S. Charpak, *Nat. Med.* **2011**, *17*, 893 – 898.
[151] H. C. Gerritsen, R. Sanders, A. Draaijer, C. Ince, Y. K. Levine, *J. Fluoresc.* **1997**, *7*, 11 – 15.
[152] J. W. Dobrucki, *J. Photochem. Photobiol. B* **2001**, *65*, 136 – 144.
[153] W. Zhong, P. Urayama, M.-A. Mycek, *J. Phys. D Appl. Phys.* **2003**, *36*, 1689 – 1695.
[154] J. K. Asiedu, J. Ji, M. Nguyen, N. Rosenzweig, Z. Rosenzweig, *J. Biomed. Opt.* **2001**, *6*, 116 – 121.
[155] J. Ji, N. Rosenzweig, I. Jones, Z. Rosenzweig, *J. Biomed. Opt.* **2002**, *7*, 404 – 409.
[156] H. Komatsu, K. Yoshihara, H. Yamada, Y. Kimura, A. Son, S.-i. Nishimoto, K. Tanabe, *Chem. Eur. J.* **2013**, *19*, 1971 – 1977.
[157] M. S. Lowry, S. Bernhard, *Chem. Eur. J.* **2006**, *12*, 7970 – 7977.
[158] S. J. Zhang, M. Hosaka, T. Yoshihara, K. Negishi, Y. Iida, S. Tobita, T. Takeuchi, *Cancer Res.* **2010**, *70*, 4490 – 4498.
[159] T. Murase, T. Yoshihara, S. Tobita, *Chem. Lett.* **2012**, *41*, 262 – 263.
[160] D. F. Wilson, S. Gomi, A. Pastuszko, J. H. Greenberg, *J. Appl. Physiol.* **1993**, *74*, 580 – 589.
[161] T. K. Stepinac, S. R. Chamot, E. Rungger-Brandle, P. Ferrez, J.-L. Munoz, H. van den Bergh, C. E. Riva, C. J. Pournaras, G. A. Wagnieres, *Invest. Ophthalmol. Visual Sci.* **2005**, *46*, 956 – 966.
[162] S. A. Vinogradov, L. W. Lo, W. T. Jenkins, S. M. Evans, C. Koch, D. F. Wilson, *Biophys. J.* **1996**, *70*, 1609 – 1617.
[163] C. Barlow, D. Rorvik, J. Kelly, *Ann. Biomed. Eng.* **1998**, *26*, 76 – 85.
[164] S. A. Vinogradov, L.-W. Lo, D. F. Wilson, *Chem. Eur. J.* **1999**, *5*, 1338 – 1347.
[165] S. A. Vinogradov, E. Kim, D. F. Wilson, *Proc. SPIE* **2002**, *4626*, 193 – 200.
[166] I. Dunphy, S. A. Vinogradov, D. F. Wilson, *Anal. Biochem.* **2002**, *310*, 191 – 198.
[167] B. J. Behnke, C. A. Kindig, T. I. Musch, S. Koga, D. C. Poole, *Respir. Physiol.* **2001**, *126*, 53 – 63.
[168] C. M. Geer, B. J. Behnke, P. McDonough, D. C. Poole, *J. Appl. Physiol.* **2002**, *93*, 227 – 232.
[169] D. C. Poole, B. J. Behnke, P. McDonough, R. M. McAllister, D. F. Wilson, *Microcirculation* **2004**, *11*, 317 – 326.

[170] D. F. Wilson, W. M. F. Lee, S. Makonnen, O. Finikova, S. Apreleva, S. A. Vinogradov, *J. Appl. Physiol.* **2006**, *101*, 1648 – 1656.
[171] D. F. Wilson, W. M. F. Lee, S. Makonnen, S. Apreleva, S. A. Vinogradov, *Adv. Exp. Med. Biol.* **2008**, *614*, 53 – 62.
[172] W. Hiesinger, S. A. Vinogradov, P. Atluri, R. Fitzpatrick, J. Raymond, J. R. Frederick, R. D. Levit, R. C. McCormick, J. R. Muenzer, E. C. Yang, N. A. Marotta, J. W. MacArthur, D. F. Wilson, Y. J. Woo, *J. Appl. Physiol.* **2011**, *110*, 1460 – 5.
[173] T. V. Esipova, A. Karagodov, J. Miller, D. F. Wilson, T. M. Busch, S. A. Vinogradov, *Anal. Chem.* **2011**, *83*, 8756 – 8765.
[174] R. P. Brinas, T. Troxler, R. M. Hochstrasser, S. A. Vinogradov, *J. Am. Chem. Soc.* **2005**, *127*, 11851 – 11862.
[175] O. S. Finikova, P. Chen, Z. P. Ou, K. M. Kadish, S. A. Vinogradov, *J. Photochem. Photobiol. A* **2008**, *198*, 75 – 84.
[176] O. S. Finikova, A. Y. Lebedev, A. Aprelev, T. Troxler, F. Gao, C. Garnacho, S. Muro, R. M. Hochstrasser, S. A. Vinogradov, *ChemPhysChem* **2008**, *9*, 1673 – 1679.
[177] A. Y. Lebedev, T. Troxler, S. A. Vinogradov, *J. Porphyrins Phthalocyanines* **2008**, *12*, 1261 – 1269.
[178] A. Devor, S. Sakadzic, P. A. Saisan, M. A. Yaseen, E. Roussakis, V. J. Srinivasan, S. A. Vinogradov, B. R. Rosen, R. B. Buxton, A. M. Dale, D. A. Boas, *J. Neurosci.* **2011**, *31*, 13676 – 13681.
[179] S. M. S. Kazmi, A. J. Salvaggio, A. D. Estrada, M. A. Hemati, N. K. Shaydyuk, E. Roussakis, T. A. Jones, S. A. Vinogradov, A. K. Dunn, *Biomed. Opt. Express* **2013**, *4*, 1061 – 1073.
[180] E. Roussakis, J. A. Spencer, C. P. Lin, S. A. Vinogradov, *Anal. Chem.* **2014**, *86*, 5937 – 5945.
[181] E. G. Mik, J. Stap, M. Sinaasappel, J. F. Beek, J. A. Aten, T. G. van Leeuwen, C. Ince, *Nat. Methods* **2006**, *3*, 939 – 945.
[182] E. G. Mik, T. Johannes, C. J. Zuurbier, A. Heinen, J. H. P. M. Houben-Weerts, G. M. Balestra, J. Stap, J. F. Beek, C. Ince, *Biophys. J.* **2008**, *95*, 3977 – 3990.
[183] S. I. A. Bodmer, G. M. Balestra, F. A. Harms, T. Johannes, N. J. H. Raat, R. J. Stolker, E. G. Mik, *J. Biophotonics* **2012**, *5*, 140 – 151.
[184] J. Hynes, S. Floyd, A. E. Soini, R. O'Connor, D. B. Papkovsky, *J. Biomol. Screening* **2003**, *8*, 264 – 272.
[185] C. O'Donovan, J. Hynes, D. Yashunski, D. B. Papkovsky, *J. Mater. Chem.* **2005**, *15*, 2946 – 2951.
[186] T. C. O'Riordan, K. Fitzgerald, G. V. Ponomarev, J. Mackrill, J. Hynes, C. Taylor, D. B. Papkovsky, *Am. J. Physiol. Regul. Integr. Comp. Physiol.* **2007**, *292*, R1613 – R1620.
[187] R. I. Dmitriev, A. V. Zhdanov, G. V. Ponomarev, D. V. Yashunski, D. B. Papkovsky, *Anal. Biochem.* **2010**, *398*, 24 – 33.
[188] R. I. Dmitriev, H. M. Ropiak, D. V. Yashunsky, G. V. Ponomarev, A. V. Zhdanov, D. B. Papkovsky, *FEBS J.* **2010**, *277*, 4651 – 4661.
[189] R. I. Dmitriev, H. M. Ropiak, G. V. Ponomarev, D. V. Yashunsky, D. B. Papkovsky, *Bioconjugate Chem.* **2011**, *22*, 2507 – 2518.
[190] K. Koren, R. I. Dmitriev, S. M. Borisov, D. B. Papkovsky, I. Klimant, *ChemBioChem* **2012**, *13*, 1184 – 1190.
[191] R. I. Dmitriev, A. V. Kondrashina, K. Koren, I. Klimant, A. V. Zhdanov, J. M. P. Pakan, K. W. McDermott, D. B. Papkovsky, *Biomater. Sci.* **2014**, *2*, 853 – 866.
[192] U. Neugebauer, Y. Pellegrin, M. Devocelle, R. J. Forster, W. Signac, N. Moran, T. E. Keyes, *Chem. Commun.* **2008**, 5307 – 5309.
[193] B. Korzeniowska, R. Nooney, D. Wencel, C. McDonagh, *Nanotechnology* **2013**, *24*, 442002.
[194] A. Ray, R. Kopelman, *Nanomedicine* **2013**, *8*, 1829 – 1838.
[195] M. P. Coogan, J. B. Court, V. L. Gray, A. J. Hayes, S. H. Lloyd, C. O. Millet, S. J. A. Pope, D. Lloyd, *Photochem. Photobiol. Sci.* **2010**, *9*, 103 – 109.
[196] P. Nowak-Sliwinska, E. Forte, H. van den Bergh, G. Wagnieres in *Photodynamic Therapy*: *Back to the Future*, SPIE, Seattle, **2009**, p. 73806N.
[197] Y.-E. K. Lee, E. E. Ulbrich, G. Kim, H. Hah, C. Strollo, W. Fan, R. Gurjar, S. Koo, R. Kopelman, *Anal. Chem.* **2010**, *82*, 8446 – 8455.
[198] A. Fercher, S. M. Borisov, A. V. Zhdanov, I. Klimant, D. B. Papkovsky, *ACS Nano* **2011**, *5*, 5499 – 5508.
[199] A. V. Kondrashina, R. I. Dmitriev, S. M. Borisov, I. Klimant, I. O'Brien, Y. M. Nolan, A. V. Zhdanov, D. B. Papkovsky, *Adv. Funct. Mater.* **2012**, *22*, 4931 – 4939.
[200] R. I. Dmitriev, S. M. Borisov, A. V. Kondrashina, J. M. P. Pakan, U. Anilkumar, J. H. M. Prehn, A. V. Zhdanov, K. W. McDermott, I. Klimant, D. B. Papkovsky, *Cell. Mol. Life Sci.* **2015**, *72*, 367 – 381.
[201] X.-H. Wang, H.-S. Peng, L. Yang, F.-T. You, F. Teng, L.-L. Hou, O. S. Wolfbeis, *Angew. Chem. Int. Ed.* **2014**, *53*, 12471 – 12475; *Angew. Chem.* **2014**, *126*, 12679 – 12683.
[202] X.-D. Wang, J. A. Stolwijk, M. Sperber, R. J. Meier, J. Wegener, O. S. Wolfbeis, *Methods Appl. Fluoresc.* **2013**, *1*, 035002.
[203] X.-D. Wang, D. E. Achatz, C. Hupf, M. Sperber, J. Wegener, S. Bange, J. M. Lupton, O. S. Wolfbeis, *Sens. Actuators B* **2013**, *188*, 257 – 262.
[204] J. Napp, T. Behnke, L. Fischer, C. Würth, M. Wottawa, D. M. Katschinski, F. Alves, U. Resch-Genger, M. Schäferling, *Anal. Chem.* **2011**, *83*, 9039 – 9046.
[205] C. F. Wu, B. Bull, K. Christensen, J. McNeill, *Angew. Chem. Int. Ed.* **2009**, *48*, 2741 – 2745; *Angew. Chem.* **2009**, *121*, 2779 – 2783.
[206] J. Liu, Y. Liu, W. Bu, J. Bu, Y. Sun, J. Du, J. Shi, *J. Am. Chem. Soc.* **2014**, *136*, 9701 – 9709.
[207] G. Q. Zhang, G. M. Palmer, M. Dewhirst, C. L. Fraser, *Nat. Mater.* **2009**, *8*, 747 – 751.
[208] J. R. Griffiths, S. P. Robinson, *Br. J. Radiol.* **1999**, *72*, 627 – 630.
[209] X.-D. Wang, O. S. Wolfbeis, *Anal. Chem.* **2013**, *85*, 487 – 508.
[210] X.-D. Wang, H.-x. Chen, Y. Zhao, X. Chen, X.-r. Wang, X. Chen, *Trends Anal. Chem.* **2010**, *29*, 319 – 338.
[211] K. Kellner, G. Liebsch, I. Klimant, O. S. Wolfbeis, T. Blunk, M. B. Schulz, A. Gopferich, *Biotechnol. Bioeng.* **2002**, *80*, 73 – 83.
[212] P. Babilas, G. Liebsch, V. Schacht, I. Klimant, O. S. Wolfbeis, R.-M. Szeimies, C. Abels, *Microcirculation* **2005**, *12*, 477 – 487.
[213] S. Schreml, R. J. Meier, O. S. Wolfbeis, T. Maisch, R.-M. Szeimies, M. Landthaler, J. Regensburger, F. Santarelli, I. Klimant, P. Babilas, *Exp. Dermatol.* **2011**, *20*, 550 – 554.
[214] J. Hofmann, R. J. Meier, A. Mahnke, V. Schatz, F. Brackmann, R. Trollmann, C. Bogdan, G. Liebsch, X.-D. Wang, O. S. Wolfbeis, J. Jantsch, *Methods Appl. Fluoresc.* **2013**, *1*, 045002.
[215] A. Mahnke, R. J. Meier, V. Schatz, J. Hofmann, K. Castiglione, U. Schleicher, O. S. Wolfbeis, C. Bogdan, J. Jantsch, *J. Invest. Dermatol.* **2014**, *134*, 2339 – 2346.
[216] P. Lehner, C. Staudinger, S. M. Borisov, I. Klimant, *Nat. Commun.* **2014**, *5*, 4460.
[217] R. J. Meier, S. Schreml, X.-d. Wang, M. Landthaler, P. Babilas, O. S. Wolfbeis, *Angew. Chem. Int. Ed.* **2011**, *50*, 10893 – 10896; *Angew. Chem.* **2011**, *123*, 11085 – 11088.
[218] S. Schreml, R. J. Meier, M. Kirschbaum, S. C. Kong, S. Gehmert, O. Felthaus, S. Kuechler, J. R. Sharpe, K. Woeltje, K. T. Weib, M. Albert, U. Seidl, J. Schroeder, C. Morsczeck, L. Prantl, C. Duschl, S. F. Pedersen, M. Gosau, M. Berneburg, O. S. Wolfbeis, M. Landthaler, P. Babilas, *Theranostics* **2014**, *4*, 721 – 735.

Received: October 31, 2014
Revised: January 5, 2015
Published online: June 17, 2015

